

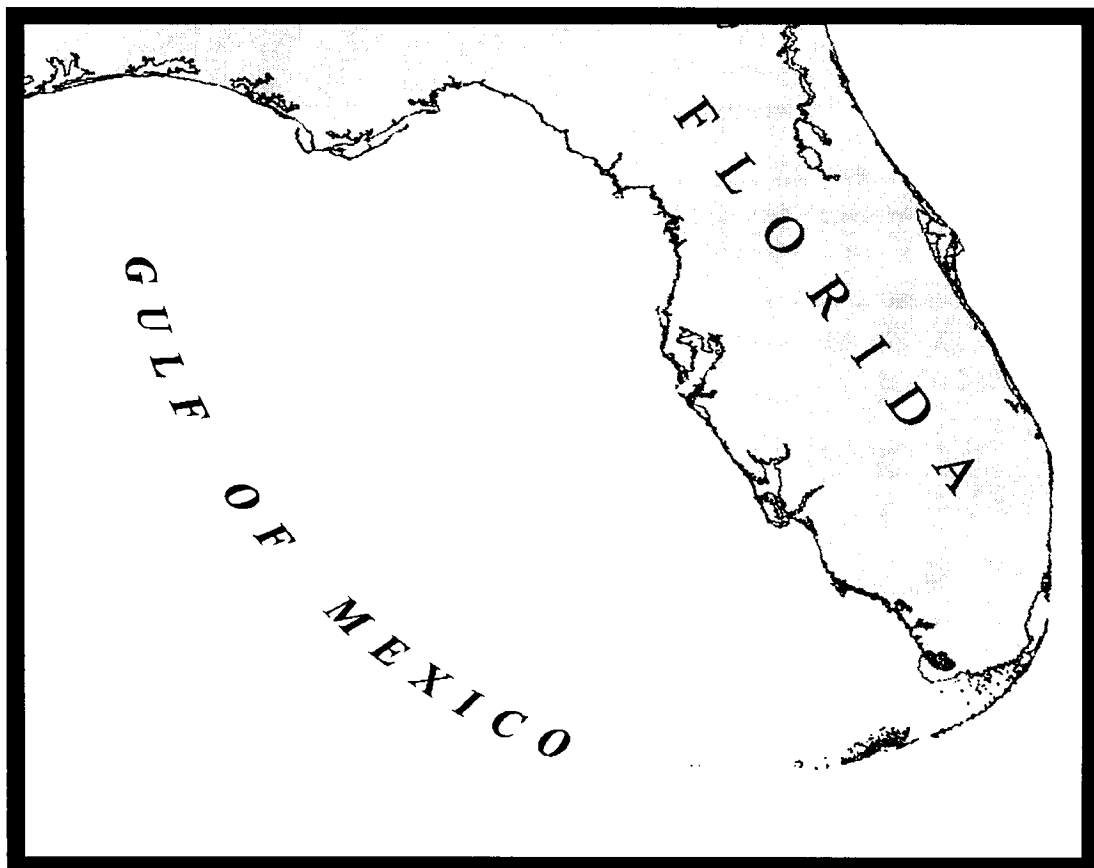


Northeastern Gulf of Mexico



# Satellite Oceanography Study and Oceanic Atlas Project

## Final Report



U.S. Department of the Interior  
Minerals Management Service  
Gulf of Mexico OCS Region

Northeastern Gulf of Mexico

# Satellite Oceanography Study and Oceanic Atlas Project

## Final Report

### Authors

Kendall L. Carder  
Frank Muller-Karger  
Robert H. Weisberg  
Richard Stumpf  
Bryan D. Black  
Christopher Cattrall

Prepared under MMS Cooperative Agreement  
14-35-0001-30767

by  
University of South Florida  
Department of Marine Science  
St. Petersburg, Florida

### Published by

**U.S. Department of the Interior**  
Minerals Management Service  
Gulf of Mexico OCS Region

New Orleans  
January 1998

## **DISCLAIMER**

This report was prepared under contract between the University of South Florida, Department of Marine Science, United States Geological Survey (USGS), and Minerals Management Service (MMS). This report has been technically reviewed by the MMS, and it has been approved for publication. Approval does not signify that the contents necessarily reflect the views and policies of the MMS, nor does mention of trade names or commercial products constitute endorsement or recommendation for use. It is, however, exempt from review and compliance with the MMS editorial standards.

## **REPORT AVAILABILITY**

Extra copies of this report may be obtained from the Public Information Office (Mail Stop 5034) at the following address:

U.S. Department of the Interior  
Minerals Management Service  
Gulf of Mexico OCS Region  
Public Information Office (MS 5034)  
1201 Elmwood Park Boulevard  
New Orleans, Louisiana 70123-2394

Telephone: (504) 736-2519 or  
1-800-200-GULF

## **CITATION**

Suggested citation:

Carder, K. L., F. Muller-Karger, R. H. Weisberg, R. Stumpf, B. D. Black, and C. Cattrall. 1997. Northeastern Gulf of Mexico Satellite Oceanography Study Final Report. OCS Study/MMS 97-0042. U.S. Dept. of the Interior, Minerals Mgmt. Service, Gulf of Mexico OCS Region, Office, New Orleans, LA xv + 44 pp.

## **ACKNOWLEDGMENTS**

The authors are expressly acknowledged for their contributions to the atlas. These include the principal investigators, Drs. Kendall Carder, Frank Muller-Karger, Richard Stumpf and Robert Weisberg, and especially USF students Bryan Black, Christopher Cattrall, and Fernando Gilbes. In addition to that provided by the authors, imagery was contributed by Herschel Hochmann, Dr. Robert Arnone, Dr. Robert Leben, Dr. Lawrence Rowse, Dr. Wilton Sturges and Dr. Frederick Vukovich. The principal investigators are grateful to the Minerals Management Service for support under MMS Co-operative Agreement 14-35-0001-30767 which was initiated by Dr. Murray Brown with oversight provided by Dr. Alexis Lugo-Fernandez through the MMS Gulf of Mexico OCS Regional Office.

## EXECUTIVE SUMMARY

Satellite and aircraft imagery of the northeastern Gulf of Mexico are presented as a visualization of patterns resulting from ocean circulation. They depict ocean fronts, eddies, meanders, streaklines, and sea-surface topography that are apparent in thermal, color, and altimetry images. The atlas is intended to provide background information useful in resource management, research, and education.

Thermal contrast between the Loop Current and adjacent waters is maximal during the winter, while ocean color contrast is maximal in the summer. Together, they provide the means of observing circulation features during the entire year. Topographic highs in excess of 50 cm above sea level are observed in the altimetry data from TOPEX and ERS1 sensors at the core of the warm, clear, Loop Current, which rotates anticyclonically (clockwise) in the southeastern part of the Gulf of Mexico. This current couples with colder, chlorophyll-rich cyclones (clockwise eddies), located adjacent to the Loop Current. Depending upon how far the Loop Current periodically penetrates into the Gulf of Mexico, the Loop Current and adjacent eddies can control much of the circulation on the outer shelves.

The inner shelf circulation patterns are usually dominated by wind-driven circulation and river outflows, with turbidity streaklines providing a means of observing the effects of coastal circulation patterns. A wide variety of flow features are depicted in the satellite imagery of the Gulf of Mexico, and special attention is paid to observations affecting the northeastern region.

## TABLE OF CONTENTS

Disclaimer Page .....	iii
Acknowledgments .....	v
Executive Summary .....	vii
List of Figures .....	xi
 I. Introduction .....	1
Physical Characteristics .....	2
Biological Characteristics .....	3
 II. Remote Sensing Methods and Characteristics .....	6
Advanced Very High Resolution Radiometer (AVHRR) .....	6
Optical Remote Sensing .....	6
Coastal Zone Color Scanner (CZCS) .....	6
Advanced Very High Resolution Radiometer (AVHRR) .....	7
Airborne Visible-Infrared Imaging Spectrometer (AVIRIS) .....	8
Altimetry .....	8
 III. Processes Assessed via Remote Sensing .....	11
Large Scale Circulation .....	11
Eddy Separation and Shedding from the Loop Current .....	11
Estuarine Processes .....	15
West Florida Shelf Interaction .....	18
Loop Current Influence upon the Shelf via Both Eddy Formation and Strong Weather System Induced Ekman Transport .....	18
A Narrow Band of Coastal Upwelling Owing to the Coalescence of Ekman Induced upwelling off of Key West/Dry Tortugas and off of Pinellas/Manatee/Sarasota counties .....	18
Banded SST and Baroclinic Structures Owing to Wind-forced Coastal Jets .....	18
Examples of Hurricanes and Tropical Storms in the Northeastern Gulf of Mexico .....	26
Biological Processes .....	28
Seasonal Chlorophyll Pigment Concentration and SST Cycles of the Gulf of Mexico .....	28
Introduction .....	28
Pigment Concentrations .....	28
Sea-surface Temperature .....	29
Sampling Notes .....	29
Chlorophyll Characteristics .....	29
Plume and Loop Current Recognition .....	30

Biological Productivity .....	31
Weekly SST Composites .....	32
SST and Pigment Concentration Complementary .....	32
River Plume Productivity .....	33
Introduction .....	33
Occurrence and Lifetime of the West Florida Plume .....	33
Processes Responsible for the Formation of the West Florida Plume	37
Local Rivers .....	37
Water Circulation .....	38
Loop Current Intrusions .....	38
Mississippi and Mobile Rivers' Discharge .....	38
Summary .....	39
Geological Processes .....	40
References .....	43

## List of Figures

Figure 1	A monthly composite of SST derived from AVHRR imagery of the Gulf of Mexico for January 1996 .....	2
Figure 2	A monthly composite of chlorophyll pigment concentration derived from CZCS imagery of the Gulf of Mexico for December 1980 .....	3
Figure 3	A monthly composite of SST derived from AVHRR imagery of the Gulf of Mexico for July 1994 .....	4
Figure 4	A monthly composite of chlorophyll pigment concentration derived from CZCS imagery of the Gulf of Mexico for June 1980 .....	5
Figure 5	A monthly composite of chlorophyll pigment concentration derived from CZCS imagery of the Gulf of Mexico for May 1980 .....	5
Figure 6	A monthly composite of the light attenuation at 490 nm derived from CZCS imagery of the Gulf of Mexico for December 1982 .....	5
Figure 7	A monthly composite of the light attenuation at 490 nm derived from CZCS imagery of the Gulf of Mexico for January 1983 .....	5
Figure 8	A composite of the dynamic height anomaly in the Gulf of Mexico derived from TOPEX/POSEIDON and ERS-1 for December 15 to December 25, 1994 .....	9
Figure 9	A monthly composite of chlorophyll pigment concentration derived from CZCS imagery of the Gulf of Mexico for August 1979 ....	11
Figure 10	A composite of SST in the Gulf of Mexico derived from AVHRR imagery for December 15 to December 25, 1994 .....	11
Figure 11	A time series of SST imagery derived from AVHRR imagery for January through March 1995 .....	12
Figure 12	A monthly composite of SST derived from AVHRR imagery of the Gulf of Mexico for July 1982 .....	12
Figure 13	A histogram of separation periods (months) of Loop Current eddies .....	13
Figure 14	A histogram of the separation month of Loop Current eddies .....	13

Figure 15	Westward paths that the Loop Current eddies have historically followed	13
Figure 16	A composite of the dynamic height anomaly in the Gulf of Mexico derived from TOPEX/POSEIDON and ERS-1 overlaid upon a composite of SST derived from AVHRR imagery of the Gulf of Mexico for December 15 to December 25, 1994 .....	14
Figure 17	An AVIRIS image of Looe Key showing bottom reflectance and resuspended sediments .....	15
Figure 18	A graph of reflectance as a function of distance and wavelength for transect line 77 shown in Figure 17.....	16
Figure 19	A graph of reflectance as a function of distance and wavelength for transect line 226 shown in Figure 17 .....	16
Figure 20	A graph of reflectance as a function of distance and wavelength for transect line 320 shown in Figure 17 .....	16
Figure 21	A map of the model-derived backscattering coefficient at 671 nm for a Tampa Bay AVIRIS overflight .....	16
Figure 22	A map of the absorption coefficient at 415 nm for a Tampa Bay AVIRIS overflight .....	16
Figure 23	A map of surface salinity derived from a Tampa Bay AVIRIS overflight	17
Figure 24	Low pass filtered time series of SST and 5 m velocity from the USF buoy, wind velocity from the NOAA buoy and sea level from St. Petersburg, FL for March 1994 .....	20
Figure 25	An SST image on the West Florida Shelf for March 4, 1994 derived from AVHRR imagery .....	21
Figure 26	An SST image on the West Florida Shelf for March 18, 1994 derived from AVHRR imagery .....	21
Figure 27	Low pass filtered time series of SST and 5 m velocity from the USF buoy, wind velocity from the NOAA buoy and sea level from St. Petersburg, FL for May 1994 .....	22
Figure 28	An SST image on the West Florida Shelf for May 22, 1994 derived from AVHRR imagery .....	23

Figure 29	Low pass filtered time series of SST and 5 m velocity from the USF buoy, wind velocity from the NOAA buoy and sea level from St. Petersburg, FL for October 1994 .....	24
Figure 30	An SST image on the West Florida Shelf for October 8, 1994 derived from AVHRR imagery .....	25
Figure 31	An SST image on the West Florida Shelf for October 21, 1994 derived from AVHRR imagery .....	25
Figure 32	SST images derived from AVHRR imagery of the West Florida Shelf showing conditions before and after the passage of Hurricane Erin .....	27
Figure 33	A map showing the location of two 200-km square subregions of the Gulf of Mexico studied using CZCS .....	29
Figure 34	A monthly climatology of pigment concentration ( $\text{mg pigment m}^{-3}$ ) and SST within the two studied subregions .....	30
Figure 35	A monthly composite of chlorophyll pigment concentration derived from CZCS imagery of the Gulf of Mexico for November 1982 .....	30
Figure 36	A monthly composite of chlorophyll pigment concentration derived from CZCS imagery of the Gulf of Mexico for February 1980 .....	30
Figure 37	A time series of monthly discharge ( $\text{m}^3 \text{s}^{-1}$ ) values for the Mississippi River as measured at Vicksburg, Mississippi .....	32
Figure 38	A CZCS time series of the West Florida Shelf showing the formation of the West Florida plume during March 1979 .....	33
Figure 39	A CZCS image of the West Florida Shelf showing the West Florida plume on March 15, 1979 .....	33
Figure 40	A CZCS image of the West Florida Shelf showing the West Florida plume on March 20, 1979 .....	34
Figure 41	A CZCS image of the West Florida Shelf showing the West Florida plume on April 1, 1979 .....	34

Figure 42	A CZCS time series of the West Florida Shelf showing the formation of the West Florida plume in late April through early June 1980 .....	34
Figure 43	A CZCS image of the West Florida Shelf showing the West Florida plume on April 24, 1980 .....	35
Figure 44	A CZCS image of the West Florida Shelf showing the West Florida plume on May 16, 1980 .....	35
Figure 45	A CZCS image of the West Florida Shelf showing the West Florida plume on May 19, 1980 .....	35
Figure 46	A CZCS image of the West Florida Shelf showing the West Florida plume on February 27, 1981 .....	35
Figure 47	A CZCS image of the West Florida Shelf showing the West Florida plume on February 24, 1982 .....	36
Figure 48	A CZCS image of the West Florida Shelf showing the West Florida plume on May 5, 1983 .....	36
Figure 49	A CZCS image of the West Florida Shelf showing the West Florida plume on April 18, 1984 .....	36
Figure 50	A CZCS image of the West Florida Shelf showing the West Florida plume on June 2, 1985 .....	36
Figure 51	A CZCS image of the West Florida Shelf showing the West Florida plume on March 7, 1986 .....	37
Figure 52	Mean total discharge ( $m^3 s^{-1}$ ) for the rivers on the northwest coast of Florida, and the southwest coast of Florida, the Mississippi River and the Mobile River for 1979 - 1985 .....	37
Figure 53	Reflectance of the Mobile Bay region measured using AVHRR for March 24, 1990 .....	40
Figure 54	Reflectance of the Mobile Bay region measured using AVHRR for March 25, 1990 .....	40
Figure 55	Reflectance of the Mobile Bay region measured using AVHRR for March 26, 1990 .....	41

Figure 56	Reflectance of the Mobile Bay region measured using AVHRR for March 27, 1990 .....	41
Figure 57	Suspended sediment load of the Mobile Bay region derived from afternoon AVHRR images for April 3, 1990 .....	41
Figure 58	Suspended sediment load of the Mobile Bay region derived from morning AVHRR images for April 4, 1990 .....	41
Figure 59	Suspended sediment load of the Mobile Bay region derived from afternoon AVHRR images for April 4, 1990 .....	42
Figure 60	Suspended sediment load of the Mobile Bay region derived from morning AVHRR images for April 5, 1990 .....	42
Figure 61	Suspended sediment load of the Mobile Bay region derived from afternoon AVHRR images for April 5, 1990 .....	42

## I. Introduction

Remote sensing via satellites, though only recently a viable technology, has produced vast amounts of data on the Earth's oceans, and the biogeophysical processes that affect them. Many researchers have entered this field, producing numerous databases on separate oceanic features or characteristics, or small collections of images depicting specific events. A need exists, however, for a comprehensive view of any part of the world's oceans that portrays, as a whole, many of the salient oceanographic features. These include sea-surface height and temperature, circulation, primary productivity and effects incurred from variations of natural processes. A corresponding survey relating several aspects of remote sensing would also be very useful.

This project attempts to address some of these deficiencies, if only for a small part of the Earth's water resource: the northeastern Gulf of Mexico. Its purpose is to synthesize, from existing research and analysis archives, a digital CD-ROM atlas of satellite remote sensing images of this area. The goal is to provide a useful tool for resource management, education, and research by providing a climatology of physical processes observable from satellites. Oceanographic features seen in satellite images attributable to the physical ecology of the region are to be depicted.

The Atlas of the Gulf of Mexico briefly introduces the reader to the use of remote sensing for studying the behavior and climatology of the Loop Current and its interaction with the waters of the Gulf of Mexico. Observations and descriptions of thermal and optical imagery are provided. These can be used to infer information about currents, heat transport, suspended sediment, and phytoplankton concentrations.

The atlas is designed to supply background information valuable to resource management, interdisciplinary products, researchers, and students (including high school). The atlas is divided into two parts:

1. Hard copy with text and basic images (no movie loops) and
2. Compact Disc, Read Only Memory (CD-ROM) complete with hypertext background and research applications supplemented by color images, movie loops, and an appendix of additional images, providing more detail.

**Physical Characteristics:** The most distinctive circulation feature in the Gulf of Mexico is the Loop Current. This can be seen clearly using Advanced Very High Resolution Radiometer (AVHRR) imagery in the winter when the temperature gradients are sharp. The origin of the Loop Current is external to the Gulf of Mexico. The North Equatorial Current, which is the southern leg of the north Atlantic subtropical gyre, flows west into the Caribbean Sea. These

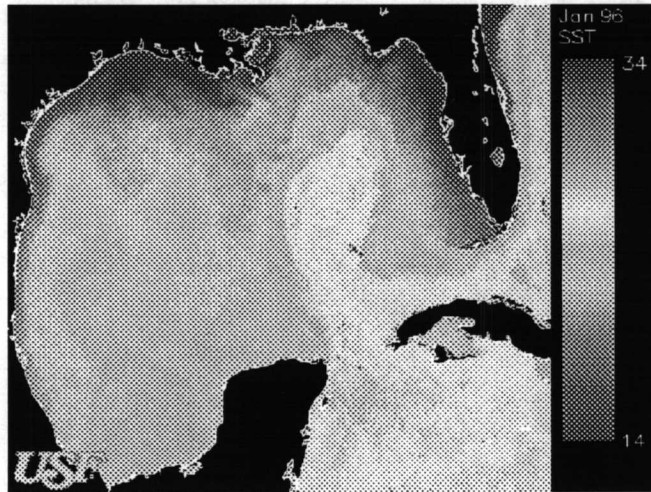


**Figure 1** A monthly composite of SST derived from AVHRR imagery of the Gulf of Mexico for January 1996

waters then enter the Gulf of Mexico through the Yucatan Channel forming the Loop Current. This current makes a clockwise loop as it moves through the Gulf and exits out of the Straits of Florida. The Loop Current is inherently unstable, and its northern extent changes with time, producing warm-core eddies that spin off with a periodicity of about 13 months (e.g., Sturges, 1994) providing oligotrophic waters to the western portion of the Gulf. As the Loop Current extends north and east, its influence on the West Florida Shelf increases. For example, by providing a dynamic height high near the Louisiana coast, it effectively drives relatively fresh, nutrient rich, waters from the Mississippi Delta onto the West Florida Shelf. While the Loop Current itself does not flow onto the shelf, waters from the Loop Current may be transported onto the shelf via the formation of smaller scale filaments or by Ekman transport. Thus, the Loop Current may be an important factor influencing the shelf circulation without flowing directly on the shelf (e.g., Weisberg et al., 1996).

**Biological Characteristics:** Water from the Caribbean flows through the Yucatan Channel into the Gulf, loops clockwise, and exits through the Florida Straits to become part of the Gulf Stream. This physical behavior is quite constant, though the depth of intrusion into the Gulf and the frequency with which eddies are formed and shed from the main Loop Current vary dramatically from year to year. The biological activity and sea-surface temperature (SST), however, change markedly over the course of a single year. In the winter months, warm water from the Caribbean forms sharp temperature gradients as it intrudes into the colder Gulf of Mexico waters (Figure 1). This Caribbean water is always low in chlorophyll pigments due to its nutrient-poor source waters. Pigment concentrations in the deep Gulf waters, however, reach a maximum at this time as the winter overturning of the surface waters mixes downwards and brings the nutrient rich waters from below (Figure 2). Later, in the spring, river discharge into the

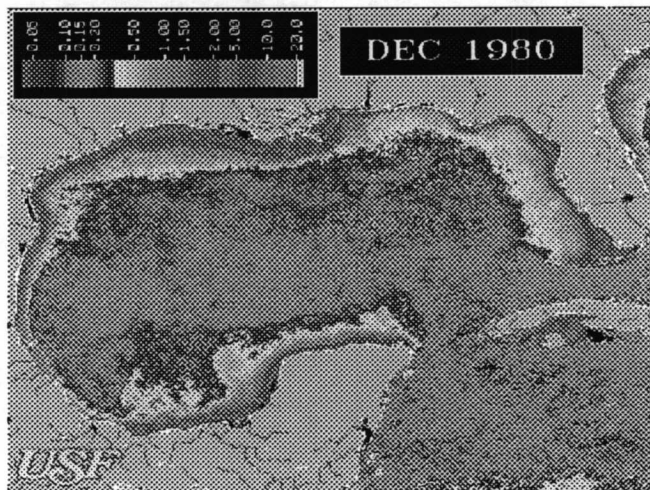


**Figure 2** A monthly composite of chlorophyll pigment concentration derived from CZCS imagery of the Gulf of Mexico for December 1980

coastal waters increases nutrient supply to the phytoplankton, allowing maximum growth during these months. Phytoplankton growth increases simultaneously across the Gulf. Thus, during these colder months, sea-surface temperature is more effectively used than chlorophyll pigment concentration as a Loop Current tracer. Pigment concentrations, while high in the winter, do not have the horizontal structure necessary to effectively trace flows in remote-sensing imagery.

During summer, the temperature of the Gulf waters reaches a maximum between July and September. These increases reduce the previous temperature contrast between the Loop Current and Gulf waters, making them indistinguishable using SST imagery as seen in Figure 3. The pigment-poor Loop Current water, however, extends farthest into the Gulf at this time of year. The chlorophyll pigment concentration, while declining from its spring value due to less river discharge (hence lower nutrient availability), is still great enough to be easily distinguishable from the very clear Caribbean waters that now extend quite deeply into the Gulf (Figure 4). Thus, while horizontal gradients in biological processes are most clearly seen during summer from

satellites, a combination of SST and chlorophyll pigment concentration imagery allow for year-round observation of near-surface processes caused by flow dynamics within the Gulf of Mexico.

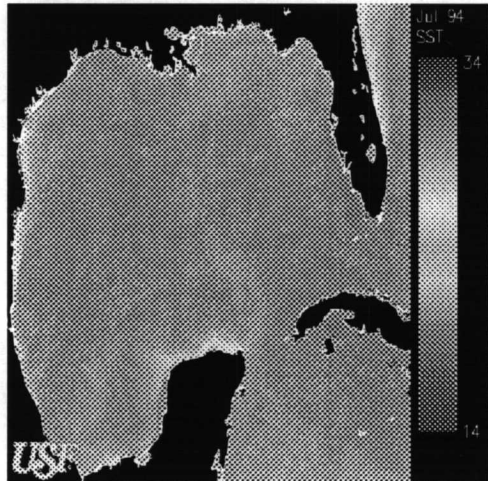


**Figure 3** A monthly composite of SST derived from AVHRR imagery of the Gulf of Mexico for July 1994

**River Plume Biology:** Sea-surface temperature and chlorophyll pigment concentration are also excellent indicators of river plumes and discharges. Coastal Zone Color Scanner (CZCS) data shown in Figure 5, clearly show that large amounts of colored material enter the Gulf of Mexico via the Mississippi Delta and Mobile Bay. River discharge is high in sediment load, gelbstoff, nutrients, and chlorophyll pigments, which greatly affects the light signal emanating from the water and received at the satellite sensor. As a plume extends into the Gulf, the sediment gradually settles out, photodegradation of gelbstoff occurs, and the phytoplankton take up the accompanying nutrients. The phytoplankton are then grazed upon by autotrophic zooplankton. These effects change the reflected (backscattered light) and absorbed light with time, making the mixing patterns

nonconservative. All these effects result in a decreased light signal. Additionally, any temperature difference between the river water and Gulf water erodes as one water body mixes with the other. These effects are seen in the monthly composites, as the river plume signal degrades rapidly as it moves away from the coast. The attenuation of light within the water column is greatly affected by the presence of phytoplankton, gelbstoff, and sediment. These effects are readily seen in Figures 6 and 7 which show some of the K490 images from the CZCS, depicting light attenuation at 490 nm. Temperature, gelbstoff, and chlorophyll pigment concentration are more conservative properties than suspended sediment, and they act as reasonable tracers on 1 to 5 day time scales.

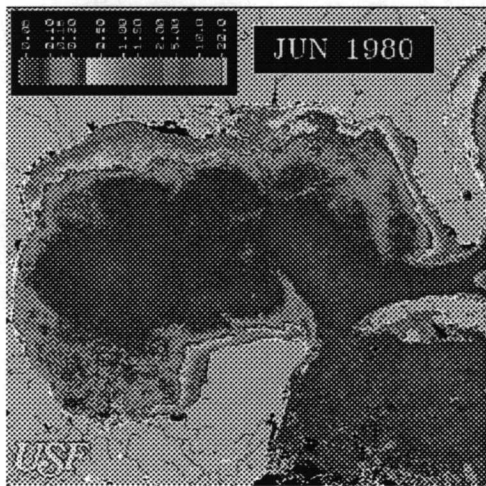


**Figure 4** A monthly composite of chlorophyll pigment concentration derived from CZCS imagery of the Gulf of Mexico for June 1980

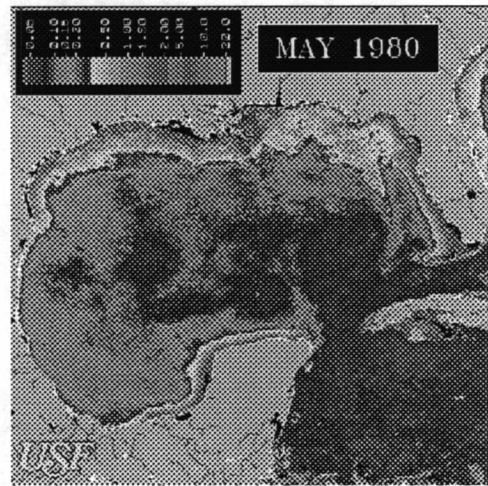


**Figure 5** A monthly composite of chlorophyll pigment concentration derived from CZCS imagery of the Gulf of Mexico for May 1980

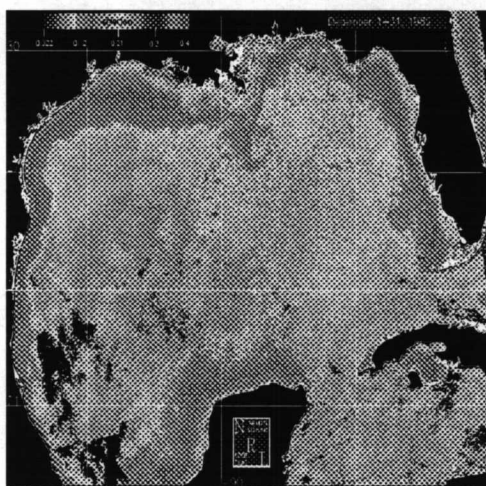


**Figure 6** A monthly composite of the light attenuation at 490 nm derived from CZCS imagery of the Gulf of Mexico for December 1982

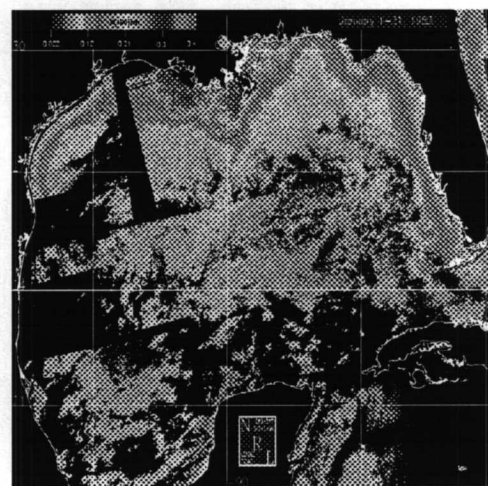


**Figure 7** A monthly composite of the light attenuation at 490 nm derived from CZCS imagery of the Gulf of Mexico for January 1983

## II. Remote Sensing Methods and Characteristics

**Advanced Very High Resolution Radiometer (AVHRR):** Water thermal properties in any region can be changed by conservative processes (mixing and advection) and by nonconservative interactions with the atmosphere (insolation, back-radiation, evaporation, condensation, and conduction; Pickard and Emery 1990). If water advects rapidly, less time is allowed for heat to be exchanged with the atmosphere, and conditions are more conservative. If the waters adjacent to a current are of a different temperature, the flow patterns are easily observed in AVHRR data. For this reason, the strong western boundary currents such as the Kuroshio and Gulf Stream currents can be observed by AVHRR. The temperature itself cannot be used directly to indicate flow, but the thermal gradients are indicative of fronts maintained by flow characteristics (see Eddy Separation and Shedding from the Loop Current).

The satellite-measured skin surface temperature (SMSST) is that of the micron-thin skin of water on top of the ocean and may not be representative of the mixed layer beneath it. The skin temperature has been observed to be between 1.2° C cooler and 0.8° C warmer than the bulk temperature (Wick et al. 1992). Multichannel sea-surface temperature (MCSST) uses comparisons between satellite infrared measurements and drifting buoys in order to determine sea-surface temperature (McClain et al. 1985). The mean offset between SMSST and MCSST is approximately 0.45° C, but without more thorough *in situ* measurements, one cannot say which method is more accurate.

Surface isotherms can be indicative of the flow path of the water, similar to slowly changing streak lines. In addition to depicting general flow characteristics of the Loop Current, warm core rings and smaller eddies, meanders, and filaments can also be clearly observed. Temporal changes in MCSST imagery provide a means of inferring some characteristics of water parcel motion and the evolution of current trajectories (e.g., Maul 1977). For more information on AVHRR go to <http://edcwww.cr.usgs.gov/glis/hyper/guide/avhrr> on the Internet.

### Optical Remote Sensing:

**Coastal Zone Color Scanner (CZCS):** The Coastal Zone Color Scanner was a scanning radiometer that viewed the ocean in six spectral bands: five (443, 520, 550, 670, 750 nm) in the visible and infrared (IR), and one in the thermal IR (10,500-12,500 nm). The CZCS, created to provide estimates of the near-surface pigment concentration with an active life of seven and a half years (1979-1986), provided an unparalleled synoptic view of the color of the world's oceans. In a sun-synchronous orbit at a nominal height of 955 km, a viewing swath width of 1,600 km and a ground resolution of 825 m was achieved. The CZCS coverage, however, was inhomogeneous with space and time, so research of oceanic processes was limited to mesoscale processes.

Several empirical facts were utilized in correcting the CZCS images for atmospheric effects and in retrieving the pigment concentration. Gordon and Clark (1981) found the water leaving radiance in the 520 and 550 nm bands could be determined *a priori* in low chlorophyll waters ( $[C] < 0.25 \text{ mg m}^{-3}$ ). Due to the strong effect of phytoplankton pigments in the blue regions, it could not be so easily determined in the 443 nm band. These two values were used to

determine the type of aerosol present between the ocean and the sensor for any clear-water portions of a scene. While the type of aerosol was assumed the same for the entire scene, the amount of aerosol could vary; this was determined at 670 nm, where the water-leaving radiance was usually less than one digital number (water was assumed to be black). If no clear water was found in the scene, the aerosol was assumed to be "white" (equal aerosol reflectance for all spectral bands). With the aerosol identified, and Rayleigh scattering known using computer code, the total radiance received at the sensor in the blue 443 nm waveband was used to determine the water-leaving radiance at this wavelength. Empirical observations by Gordon et al. (1983) of the relationship between the water-leaving radiances at 550 and 443 nm and pigment concentration were then used to determine the pigment (i.e., chlorophyll) concentration at the site in question.

Theoretically, CZCS images should allow recovery of the blue water-leaving radiance to within 10-15% and the pigment concentration to within 30-40%, under optimal conditions. Surface winds, multiple scattering, and mixing of aerosol types all work to confound pigment retrieval. Much current research is focused on quantifying these effects for the next generation of ocean-viewing sensors.

Advanced Very High Resolution Radiometer (AVHRR): The AVHRR is a part of an environmental satellite system named the TIROS-N series (launched October 1978) that was later continued as the NOAA-N series. At present, NOAA-12 and NOAA-14 are operational. The system is a result of a cooperative effort between the United States, United Kingdom, and France to provide daily environmental monitoring and to promote global change research.

Many instruments operate onboard each NOAA satellite. Of particular interest to oceanic optical remote sensing is the AVHRR. A 5-channel scanning radiometer (580-680; 725-1,100; 3,550-3,930; 10,350-11,300; 11,500-12,500 nm), it observes in the red, near infrared, and infrared parts of the spectrum at a nominal resolution of 1 km. Such resolution, however, provides a data stream too voluminous for daily capture; global area coverage is provided at 4-km resolution after the data is subsampled and averaged onboard the instrument. The NOAA-N series satellites possess two modes of operation: an afternoon ascending node (northward Equator crossing) and a descending (southward Equator crossing) node in the morning. The orbit is near-polar and sun synchronous, with a period of approximately 102 minutes (14/day); each cross-track scan corresponds to a swath width of 2,700 km. Further technical details may be found in Kidwell (1991).

The daily coverage provided by the AVHRR is a vast improvement over the sparse (weekly or worse) imagery previously obtained by sensors such as SPOT and Landsat. Such temporal frequency allows for observations and analyses of rapidly changing physical processes such as those found during floods and hurricanes, or in estuarine and near-coastal regions. The saturation radiance of the AVHRR's sensors is much greater than that of the CZCS, allowing for evaluation of quite turbid water where the total reflectance is much greater than for clear water. More information on the remote sensing of turbid estuaries and other areas may be found in the Geological Processes section. For more information on AVHRR go to <http://edcwww.cr.usgs.gov/glis/hyper/guide/avhrr>.

Airborne Visible-Infrared Imaging Spectrometer (AVIRIS): AVIRIS is a test-bed for future spacecraft imaging spectrometers such as MODIS, HIRIS, and SeaWiFS (projected launch date 1997). With 224 spectral channels between 400 and 2,400 nm and 20-m square pixels at 65,000 feet altitude, a signal-to-noise ratio of 10-20% of that of CZCS is obtained by Carder et al. (1993). Recent improvements have significantly increased responsivity of AVIRIS at the blue end (R. Greene, Jet Propulsion Laboratory; personal communication). Spatial averaging can increase the signal-to-noise ratio, at the cost of spatial resolution. Vicarious calibration must be performed on each flight by modeling the upwelling light field using computer code, such as Lowtran 7 multiple-scattering code, and accounting for the atmospheric effects. The calibrated sensor can then provide spectral values of water-leaving radiance, providing the signal-to-noise ratio is large enough.

A large advantage to this type of spectrometer is the greatly increased spatial resolution. Even a 14-fold increase in pixel signal-to-noise ratio resulted in a 280-m spatial resolution for the backscattering coefficient at 671 nm, and a 50-fold increase at 415 nm still resulted in a 1,000-m resolution for the absorption coefficient in the analysis of Carder et al. (1993) More information about performance characteristics is provided on the Internet homepage at <http://www.ophelia.jpl.nasa.gov/pub/docs/html/aboutAV.htm>.

**Altimetry:** Many factors affect ocean circulation: winds, bottom topography, sea-surface height, sea-surface temperature, and Coriolis forces resulting from the rotation of the earth. The major driver of the observed flow characteristics are differences in sea-surface height; flow resulting from these differences is called geostrophic flow, the balance between the horizontal pressure gradient and the Coriolis force. Early sensors such as Gayest and ERS-1 were designed for the remote estimation of sea-surface height in order to determine general flow characteristics, geoid values, and tidal component estimates (Andersen 1994). ERS-1 provides excellent spatial coverage of the earth, but the sea-surface height accuracy is not quite good enough to determine detailed geostrophic flow fields. This state of affairs changed remarkably with the 1992 launch of the NASA/CANES satellite TOPEX/POSEIDON, a new sea-surface height sensor of superb accuracy with an RMS error of 4.7 cm for TOPEX and 5.1 cm for POSEIDON (Fu et al., 1995). After 3 years of operation, a significant improvement in our understanding of ocean circulation has been obtained from such detailed imagery.

Using the TOPEX/POSEIDON satellite, three sea-surface height (SASH) fields can be calculated (Stammer and Wunsch, 1994):

1. instantaneous SSH;
2. time averaged (over mission) SSH; and
3. time dependent SSH-difference between (1) and (2).

The instantaneous SSH, or composites of them, are most commonly studied. Sea-surface topography is calculated relative to the earth's geoid (the earth's gravitational equipotential surface); sea-surface height is measured by the difference between the TOPEX/sea-surface height distance and the TOPEX/geoid distance. The geostrophic flow resulting from the balance between the Coriolis force and the horizontal pressure gradient produced by the dynamic height

field, shown for example in Figure 8, may then be calculated. Altimetric highs will have geostrophic velocity in the clockwise direction in the northern hemisphere, while the altimetric lows produce velocities in the anticlockwise direction.

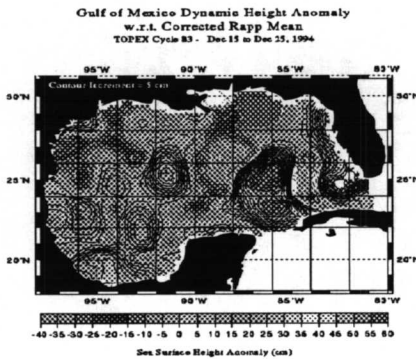


**Figure 8** A composite of the dynamic height anomaly in the Gulf of Mexico derived from TOPEX/POSEIDON and ERS-1 for December 15 to December 25, 1994

Means of SSH over the TOPEX mission have been developed that superbly illustrate the mean geostrophic flow features of the world oceans. They are remarkable in that one easily identifies many of the permanent oceanographic circulation features obtained from ship-board measurements and theory - the North Atlantic subtropical and subpolar gyres, the Antarctic Circumpolar Current, the two subtropical gyres of the Pacific Ocean, and many of the western boundary currents such as the Gulf Stream, Kuroshio and Brazil Currents. Even the extreme seasonal fluctuations of current characteristics in the Indian Ocean are evident from the very poorly defined flow patterns.

TOPEX/POSEIDON utilizes several state-of-the-art techniques and systems to determine orbital position, height, and corrective factors to the accuracy needed for good altimetric retrieval. Several will be mentioned in order to illustrate where future progress in satellite altimetry can be expected. Errors inherent to the instrumentation and techniques include measurement noise and corrections for sea state and altimeter pointing angle. A two-frequency radar altimeter present on board the satellite helps quantify, and thus correct for, free electrons present in the ionosphere that delay the signal's return to the satellite; a 3-frequency microwave sensor performs a similar task by estimating the signal delay from tropospheric water vapor.

A comparison between the TOPEX/POSEIDON yearly mean SSH and the most complete, accepted ocean circulation model of Semtner and Chervin (1992), and a fairly extensive set of hydrographic and climatological data from Levitus (1983) has shown that a 10-30 cm difference exists between satellite data and the other two methods. Strong inconsistencies were seen at continental boundaries and major trench systems. It is believed that since these areas possess

large geoid gradients, an incorrect estimation of the geoid is a likely candidate for the source of error. A consistent 25 to 35-cm discrepancy exists in the tropical/equatorial Pacific; this further suggests that the geoid is a large source of error, at least in that part of the world's oceans.

ERS-1 is not as accurate an altimetric satellite as TOPEX, but it has been used for important studies nevertheless. Observations of eddy kinetic viscosity fields of the North Atlantic subpolar gyre (Heywood et al. 1994) has yielded an excellent correlation between mean currents and bathymetric constraints. ERS-1 has a much finer spatial resolution (3/4 by 3/4 degree) than TOPEX/POSEIDON (3 by 3) and a much greater spatial coverage than its more modern counterpart. This has led ERS-1 to be used to determine tidal components that has been used to compute the SSH using TOPEX/POSEIDON. The greater spatial coverage with lesser SSH resolution has led to a technique that calibrates the ERS-1 data with TOPEX. These results are then meshed and used to obtain a final SSH product.

For more performance information on altimetry measurements in the Gulf of Mexico, please see [http://shaman.colorado.edu/~leben/gom\\_rgdr.htm](http://shaman.colorado.edu/~leben/gom_rgdr.htm).

### III. Processes Assessed via Remote Sensing

**Large Scale Circulation:** The bathymetry of the Gulf of Mexico includes major oceanic inflow and outflow ports in the south and the southeast, respectively, with most river inflow occurring along the northern boundary. Wide shelves are found along the Florida and Campeche coasts; narrower ones around the western basin. A very narrow shelf is found between Pensacola and Apalachicola, Florida, where the De Soto Canyon penetrates almost to the shoreline. Monthly composites of inferred chlorophyll concentration show the generally hot, clear waters from the Caribbean Sea flowing into and out of the Gulf of Mexico in a clockwise looping behavior.

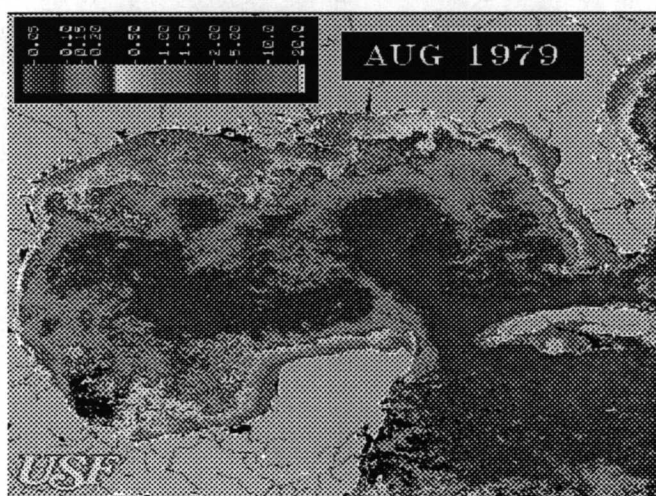


**Figure 9** A monthly composite of chlorophyll pigment concentration derived from CZCS imagery of the Gulf of Mexico for August 1979

Current: A comparison of Figure 8, satellite altimetry data from TOPEX and ERS-1 (provided by Dr. Robert Leben of the University of Colorado, corrected for orbit, geopotential, and tidal effects) of the Gulf of Mexico with ocean thermal imagery (Figure 10), shows that the SST signature of the Loop Current matches the dynamic height high shown in the altimetry imagery. Data obtained through altimetry sensors can be used to calculate the first order or geostrophic currents in the ocean. Looking at the altimetry image referenced above, we can see that the actual Loop Current is positioned around the largest dynamic height signature, where the lines of constant sea-surface height are closest together. A time-series image of scenes from January to March 1995 (Figure 11) shows the

Chlorophyll contrast for Gulf of Mexico waters is greatest in the summer which is shown in Figure 9, a CZCS image for August 1979 and least in the winter as seen in Figure 2, a CZCS image for December 1980.

Sea-surface temperature behaves in the opposite way. During the summer, the surface waters of the Gulf of Mexico are quite homogeneous. The winter months show the hot Caribbean water intruding into the cold Gulf water, creating sharp temperature gradients. Thus, a combination of chlorophyll pigment and sea-surface temperature provides a year-round look at the large-scale, surface processes occurring in the Gulf of Mexico.

#### Eddy Separation and Shedding from the Loop



**Figure 10** A composite of SST in the Gulf of Mexico derived from AVHRR imagery for December 15 to December 25, 1994

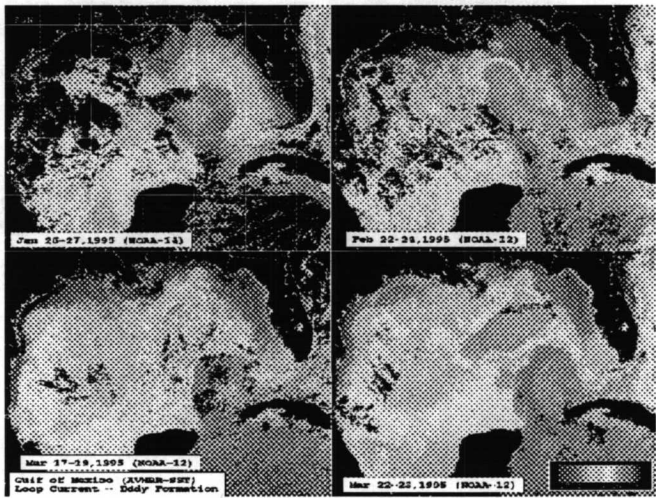


**Figure 11** A time series of SST imagery derived from AVHRR imagery for January through March 1995

separate from the main body of the Loop Current at an average of 11.3 months (Vukovich, 1995) as shown in Figure 13. He also found that the eddies were more likely to separate in the spring or summer (Figure 14). Figure 15 shows the paths the eddies have followed west since they have been studied remotely. This suggests that altimetry data combined with both ocean color and thermal imagery will better depict the circulation features than any of them separately. Effects of heat transport and exchange with the atmosphere, as well as diffusion with the adjacent waters, will be apparent in time sequences of the imagery. When appropriate models of the circulation, thermodynamics, and primary production of the Gulf need testing, initialization or updating, a combination of altimetric, thermal, and color imagery will be much more useful than just one of these. Figure 16, a composite of the sea-surface temperature overlaid upon the altimetry image shown in the previous paragraph clearly indicates the correlation of sea-surface temperature to sea-surface height in the Loop Current. The resulting observation of the warm-core eddy that separated from the Loop Current might lead to new insights on the frequency and conditions of such separation events, previously overlooked by infrequent ship data. Time series of such overlay images will provide significant understanding on the dynamics of the surface flow.

separation of a warm core eddy from the main body of the Loop Current. The altimetric highs in the Gulf have a Caribbean source, so they are warm, clock-wise circulation features in the eastern part of the basin, and the lows are cool, counter-clockwise features consisting of older Gulf water. Farther to the west, away from the Caribbean source of warm water, the thermal distinction disappears as thermal exchange with the atmosphere dominates the thermal inertia of the warm rings.

Coastal Zone Color Scanner data have depicted some rings of blue water that were transported almost to the western shelf of the basin before their low-chlorophyll signatures were lost, as seen in Figure 12. Eddies



**Figure 12** A monthly composite of SST derived from AVHRR imagery of the Gulf of Mexico for July 1982

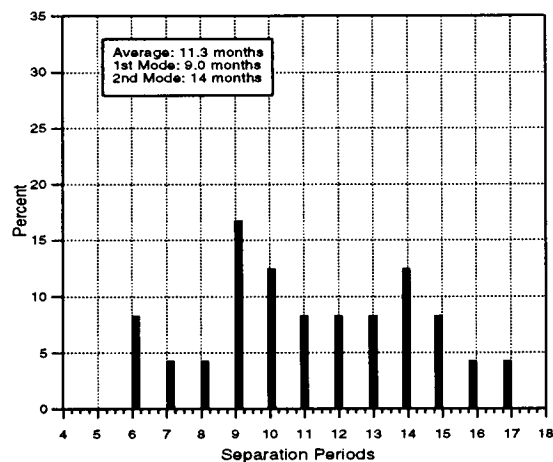


**Figure 13** A histogram of separation period (months) of Loop Current eddies

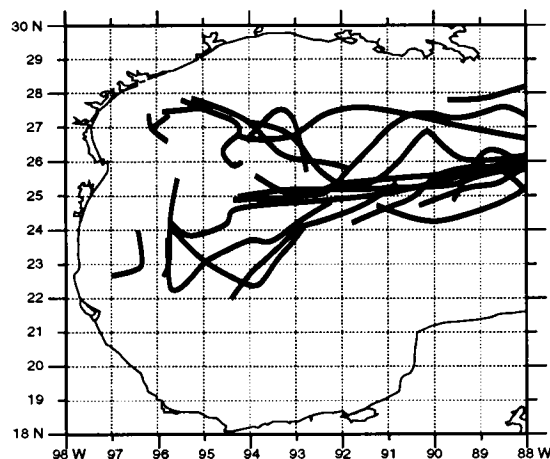


**Figure 15** Westward paths that the Loop Current eddies have historically followed

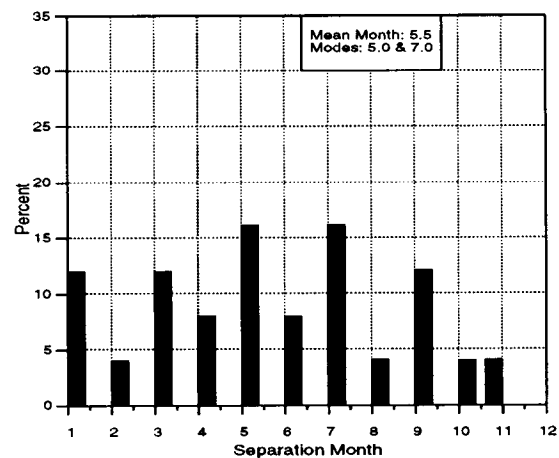


**Figure 14** A histogram of the separation month of Loop Current eddies

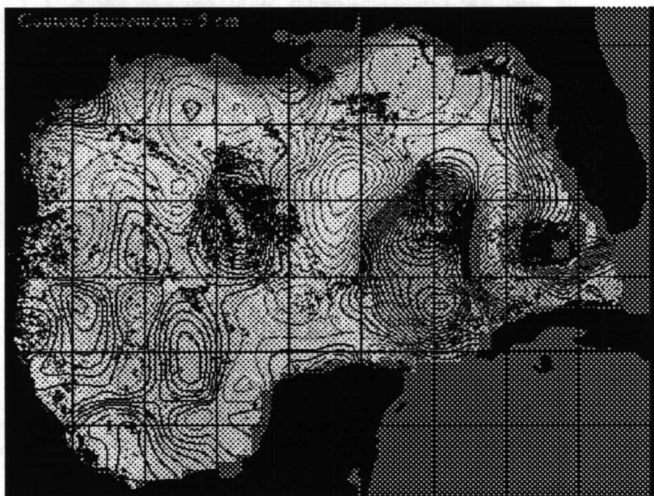


**Figure 16** A composite of the dynamic height anomaly in the Gulf of Mexico derived from TOPEX/POSEIDON and ERS-1 overlaid upon a composite of SST derived from AVHRR imagery of the Gulf of Mexico for December 15 to December 25, 1994

**Estuarine Processes:** Deriving physical processes of rivers and oceans can be achieved using the large-scale viewing capabilities of space-borne sensors such as AVHRR, CZCS, or SeaWiFS. Estuarine processes occur on a much shorter spatial and spectral scale that surpasses the resolution capabilities of such satellite platforms. These smaller scales are due to the mixing of dissolved and particulate constituents, frequent variations in absorptive, scattering and fluorescent spectral properties, and changes in the bottom topography and albedo. AVIRIS is an airborne sensor that can achieve the signal-to-noise resolution required by oceanographers, but at the spatial scales necessary to observe and interpret the near-coastal environment.

In many estuaries, conservative mixing and dilution exist, such that the derivation of the optical properties of dissolved material allows a strong prediction of the salinity of the water. Thus, since color-dissolved organic matter (gelbstoff) travels with water flow, if the absorption coefficient of such gelbstoff can be derived from the images, so may the salinity, given an accurate absorption-salinity relationship. Such relationships are presently determined by ship-board measurements; it is hoped that future oceanographic buoys moored in the mouth of such estuaries and bays will have the instrumentation required.

An AVIRIS image of Looe Key, an underwater reef structure in the Florida Keys, is shown in Figure 17 and clearly indicates the effects of bottom reflectance and resuspended sediments. The three line profiles - line 77, line 226, and line 320, shown in Figures 18, 19, and 20 respectively, illustrate the marked variations in reflectance profiles possible in just one image. The large peak in 226 over a wide spectral range is due purely to strong, fairly nonspectral,

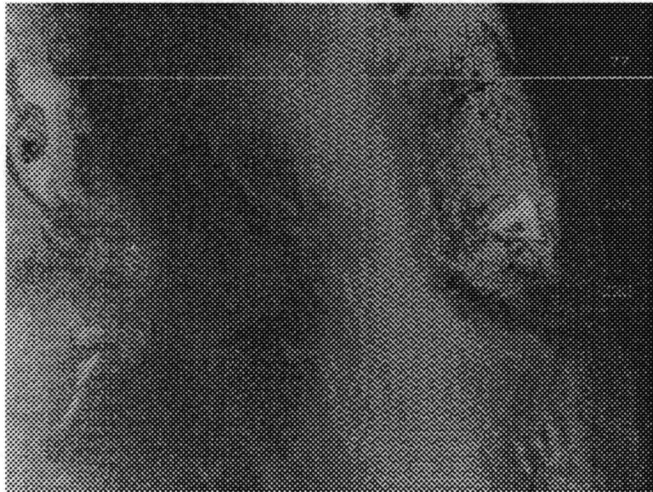


**Figure 17** An AVIRIS image of Looe Key showing bottom reflectance and resuspended sediments

bottom reflectance. Strong, sharp peaks at the red wavelengths exist in the three lines, possibly due to phytoplankton fluorescence.

In order to demonstrate the ability of AVIRIS to remotely sense salinity plumes from nearshore processes, an overflight of Tampa Bay was performed in 1990 and 1992. Maps of the model-derived backscattering coefficient at 671 nm and the absorption coefficient at 415 nm are shown in Figures 17 and 18 respectively. In nearshore environments, variation in the backscattering coefficient is significantly affected by tidally-derived suspended sediments from Tampa Bay, and local resuspensions form shoal areas. At such short wavelengths as 415 nm, the

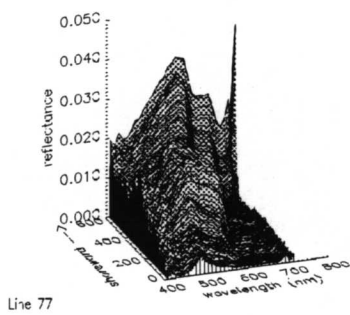


**Figure 18** A graph of reflectance as a function of distance and wavelength for transect line 77 shown in Figure 17

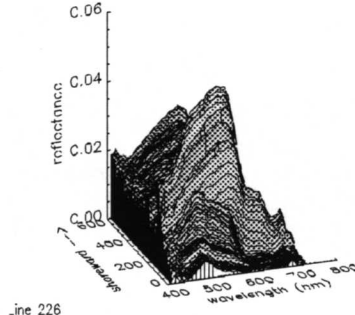


**Figure 19** A graph of reflectance as a function of distance and wavelength for transect line 226 shown in Figure 17

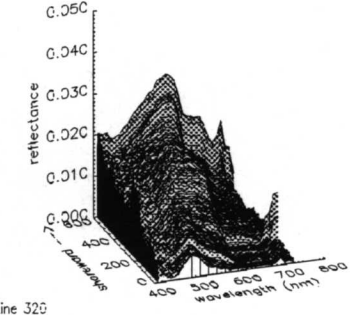


**Figure 20** A graph of reflectance as a function of distance and wavelength for transect line 320 shown in Figure 17

absorption is dominated by gelbstoff, a refractory, rather conservative constituent. The phytoplankton signal that tends to dominate at higher blue and green wavelengths is relatively small at 415 nm compared to the gelbstoff signal. This allows absorption due to gelbstoff to be determined; with a further gelbstoff/salinity relationship, a means of mapping salinity is achieved. Images of backscattering (671 nm), absorption (415 nm), and salinity, are shown in Figures 21, 22 and 23 respectively, to depict the distribution of dissolved and particulate constituents for the Tampa Bay plume during late, ebb-tidal conditions.

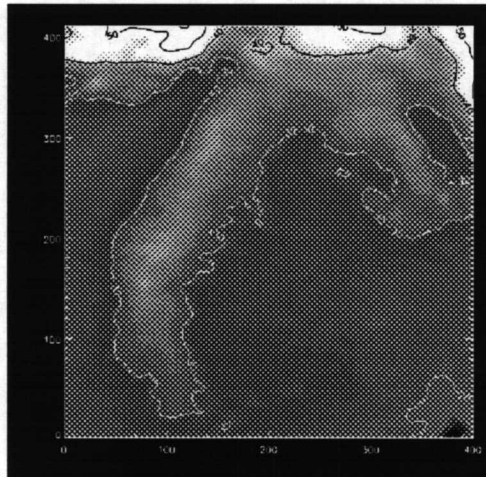


**Figure 21** A map of the model-derived backscattering coefficient at 671 nm for a Tampa Bay AVIRIS overflight

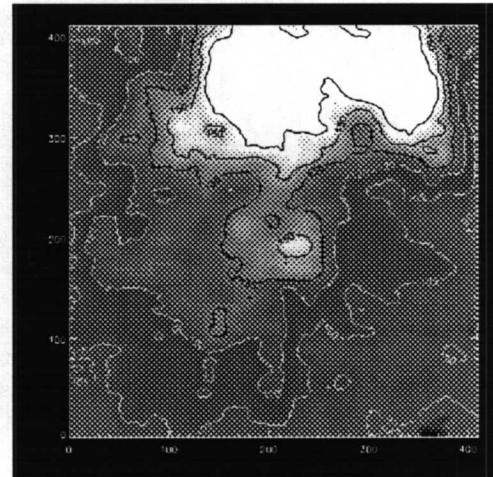


**Figure 22** A map of the absorption coefficient at 415 nm for a Tampa bay AVIRIS overflight

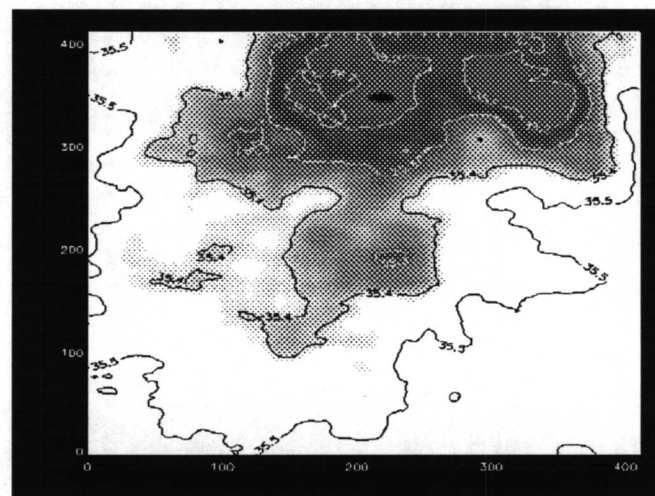


**Figure 23** A map of surface salinity derived from a Tampa Bay AVIRIS overflight

**West Florida Shelf Interaction:** Satellite AVHRR infrared images have been used to study SST patterns across the West Florida Shelf. This is an effective qualitative tool, but alone it offers little insight into ocean circulation patterns. Coupled with *in situ* hydrography, wind and current measurements these images may be used to infer possible circulation information beyond the immediate measurement site. If these components are not added to the data analysis, then three dimensionality of the current regime can not be explained. Below, we offer some examples of circulation patterns on the West Florida Shelf and some possible explanations. These explanations are offered for discussion and are not conclusive.

A current measurement program on the west-central Florida shelf has been underway since October 5, 1993. The first 16 months have been analyzed and when analyzed together with the AVHRR data, it offers some insight into the forces that drive the circulation over the west-central Florida shelf. Some examples have been offered below.

Loop Current Influence upon the Shelf via Both Eddy Formation and Strong Weather

System Induced Ekman Transport: The Loop Current is constrained from impinging directly onto the West Florida Shelf by depth related vorticity considerations. However, eddy formation and trapping of Loop Current waters on the shelf break combined with onshore Ekman transports provides a mechanism by which Loop Current waters can be transported onto the shelf. An example of this is found in March 1994. Towards the end of February, a Loop Current eddy formed near the shelf break. A storm with strong southerly winds, shown in Figure 24, facilitated the trapping of this eddy onto the shelf break, pictured in Figure 25, and an onshore wind induced transport of Loop current waters onto the shelf. Subsequent satellite imagery (Figure 26) then showed fairly steady surface conditions for the remainder of the month and indeed despite relatively weak southerly winds, the near surface currents persisted toward the south consistent with the baroclinic effect of the relatively warm Loop Current water that had made its way onto the shelf.

A Narrow Band of Coastal Upwelling Owing to the Coalescence of Ekman Induced Upwelling off of Key West/Dry Tortugas and off of Pinellas/Manatee/Sarasota Counties: Very pronounced banded SST distributions owing to coastal jets are also observed nearshore as evident in May 1994. This is a particularly interesting example because it shows an upwelling feature that is continuous from the Dry Tortugas to the Big Bend. May 1994 *in situ* data (Figure 27) show that the mid-shelf currents were southward (for baroclinic reasons) over most of the month. Strong northeasterly winds developed around May 19, which caused an offshore Ekman transport and an associated drop in sea level and SST. Prior to this a localized region of upwelling was observed on the northern side of Key West/Dry Tortugas, but otherwise SST along the coast was warm. By May 22, a very pronounced narrow band of upwelling was observed along the entire length of the coast linking the southernmost region with a maximum just off Tampa Bay (Figure 28).

Banded SST and Baroclinic Structures on the Shelf Owing to Wind-forced Coastal Jets:

For the same reasons that Loop Current intrusions are constrained by topography, the circulation along the mid-portion West Florida Shelf also tends to be along-isobath (which is essentially

along-shore). The shelf therefore responds to large scale wind forcing by forming along-shore jets. An example of this, discernable in satellite SST imagery, occurred in early October 1994 in response to a major storm. In situ data for October 1994 are presented in Figure 29. Prior to the storm SST was uniformly warm over the southern half of the shelf. After the storm a pattern of warm SST is observed to extend along the entire mid-shelf region past Cape San Blas and into the northwest portion of the shelf (Figure 30). This pattern retreated somewhat, but remained a distinctive feature sandwiched between relatively cold coastal and shelf break waters (Figure 31) before dissipating by the end of the month. Note that the cold shelf break waters mark the outer edge of the Loop Current. These waters are cold for two reasons: first, the thermocline is shallowest on the outer edge for geostrophic reasons and second, any flows occurring onshore will cause upwelling for kinematical reasons. A narrow band of cold water at the shelf break is a common occurrence on the West Florida Shelf.

Satellite SST imagery is an effective tool in recognizing surface circulation patterns, but when coupled with *in situ* measurements, its ability for describing the horizontal flow structure is improved.

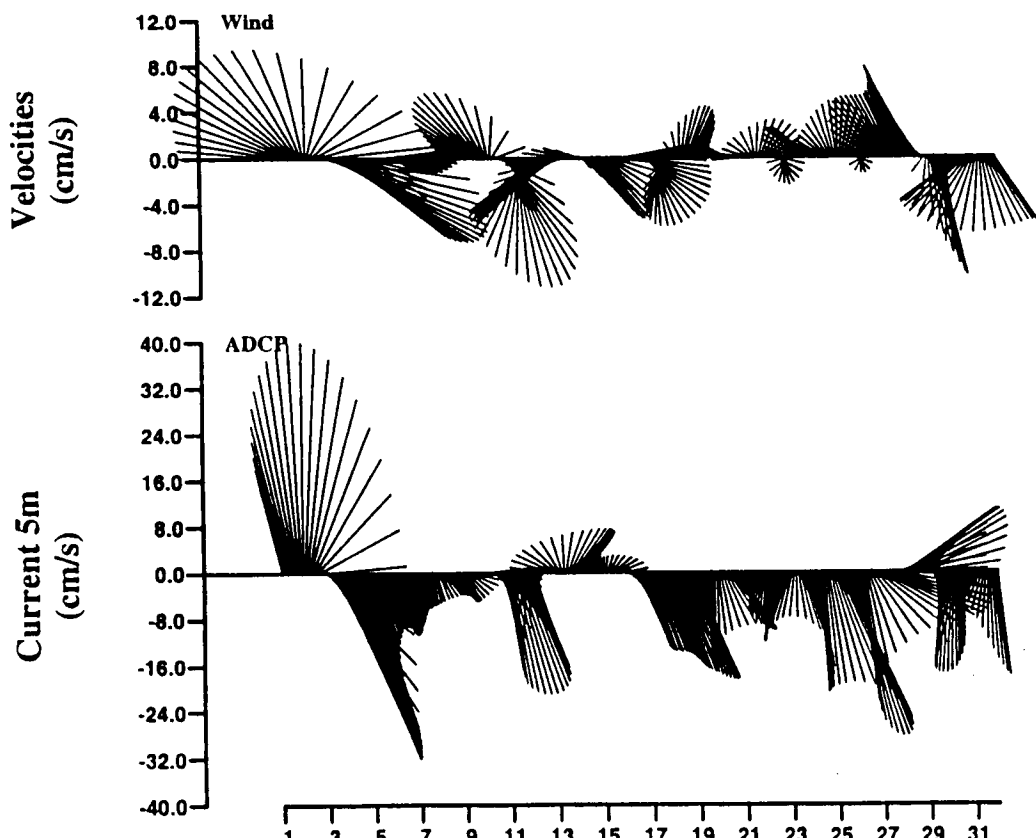
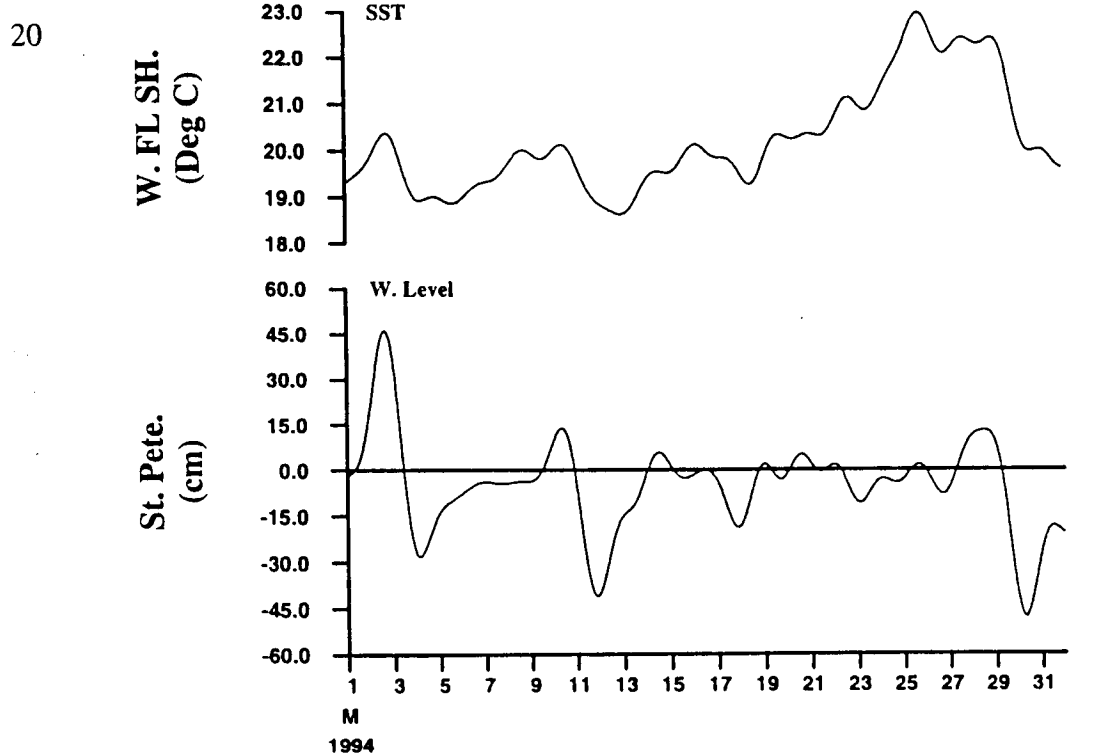


**Figure 24.** Low pass filtered time series of SST and 5m velocity from the USF buoy, wind velocity from the NOAA buoy and sea level from St. Petersburg, FL for March, 1994

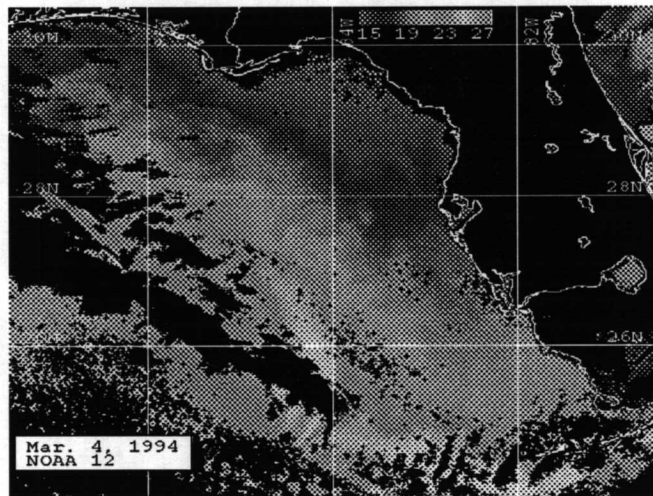


**Figure 25** An SST image of the West Florida Shelf for March 4, 1994 derived from AVHRR imagery

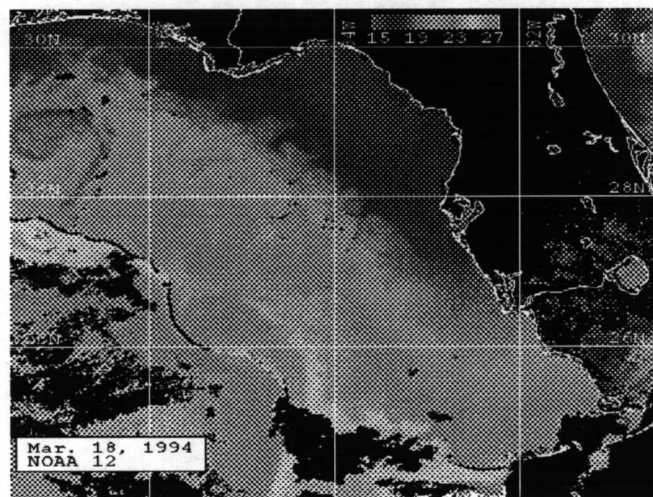


**Figure 26** An SST image of the West Florida Shelf for March 18, 1994 derived from AVHRR imagery

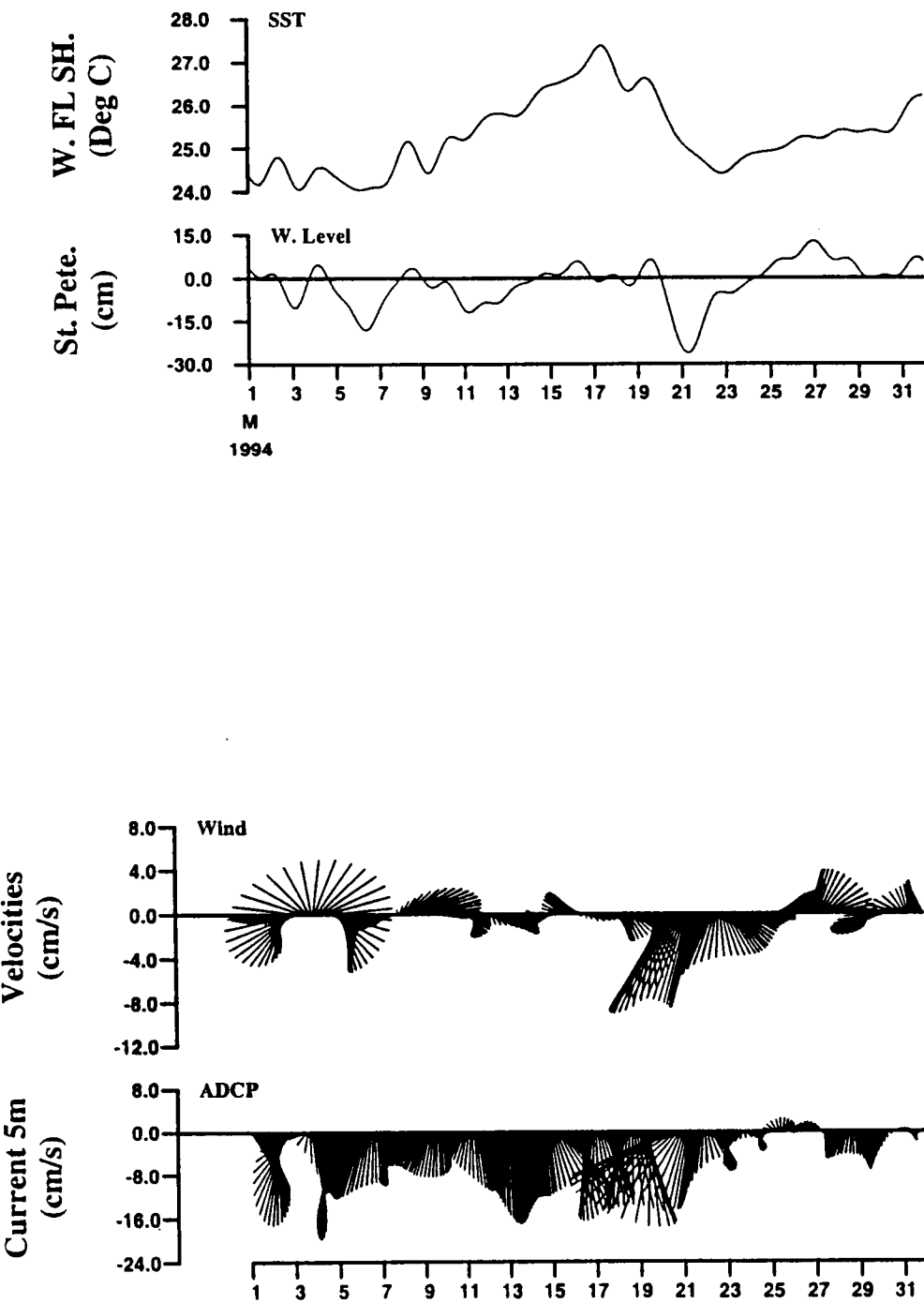


**Figure 27.** Low pass filtered time series of SST and 5m velocity from the USF buoy, wind velocity from the NOAA buoy and sea level from St. Petersburg, FL for May, 1994

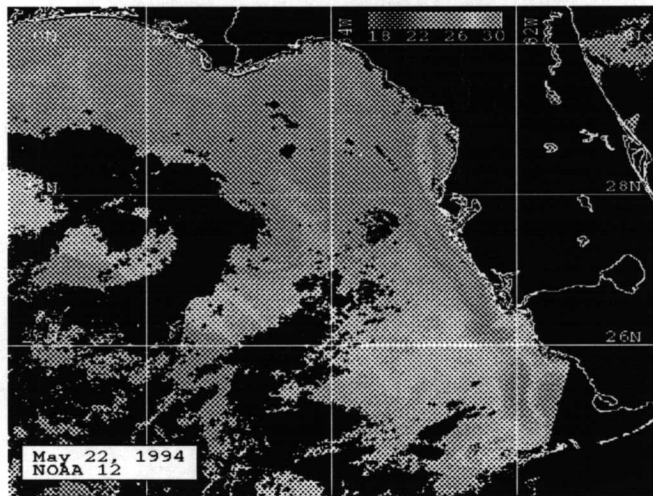


**Figure 28** An SST image of the West Florida Shelf for May 22, 1994 derived from AVHRR imagery

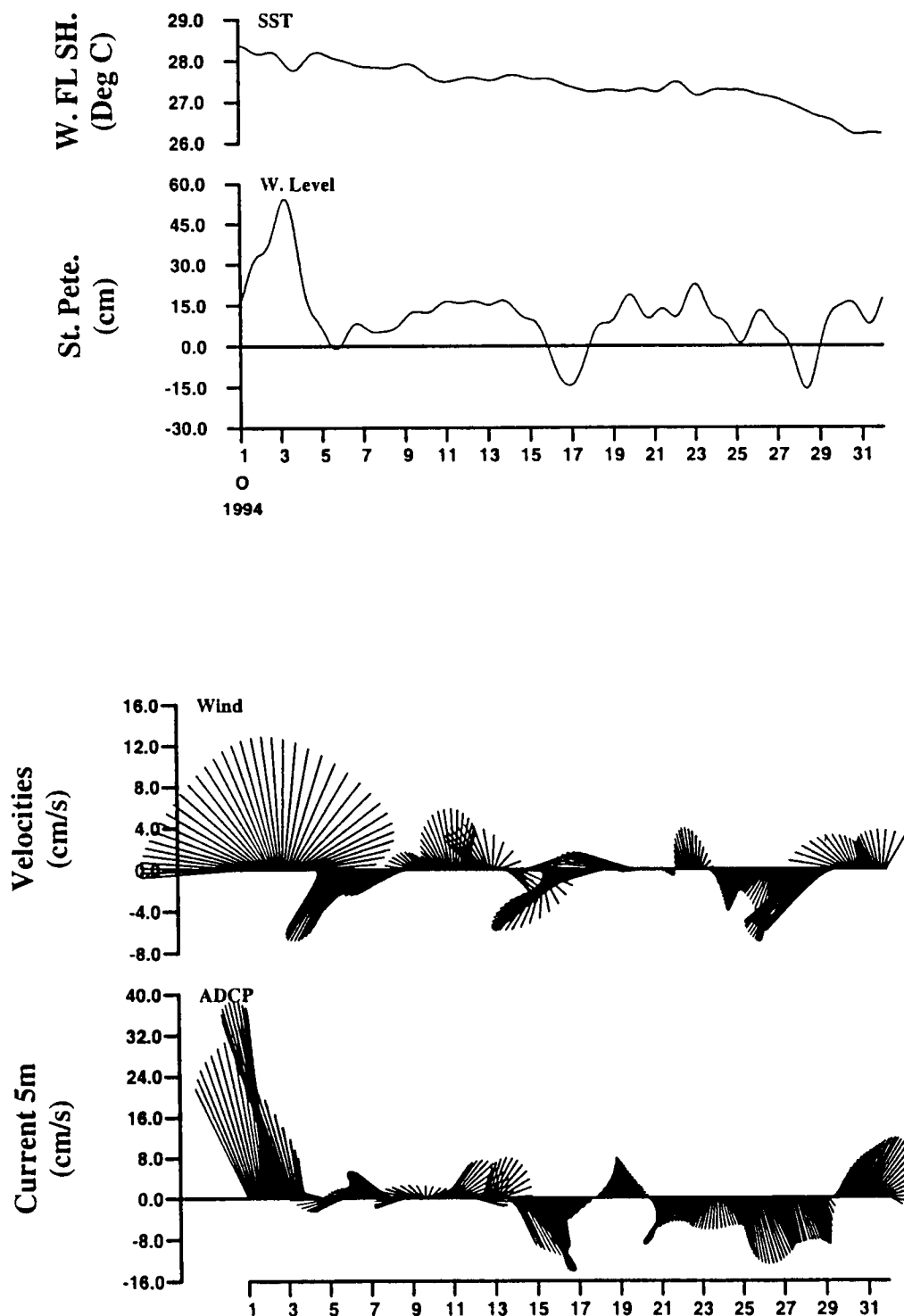


**Figure 29.** Low pass filtered time series of SST and 5m velocity from the USF buoy, wind velocity from the NOAA buoy and sea level from St. Petersburg, FL for October, 1994

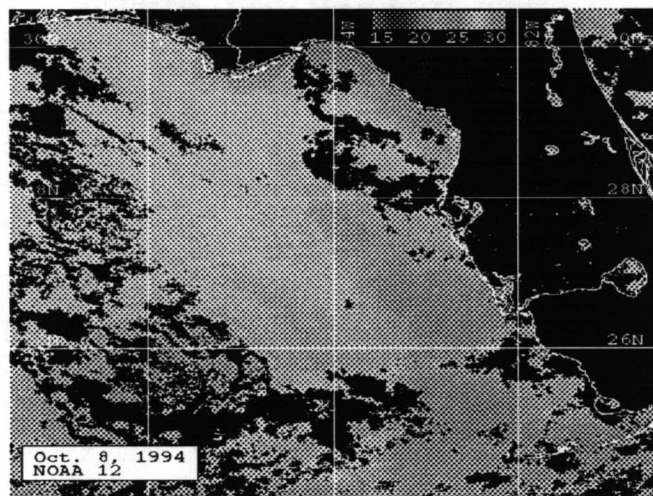


**Figure 30** An SST image of the West Florida Shelf for October 8, 1994 derived from AVHRR imagery

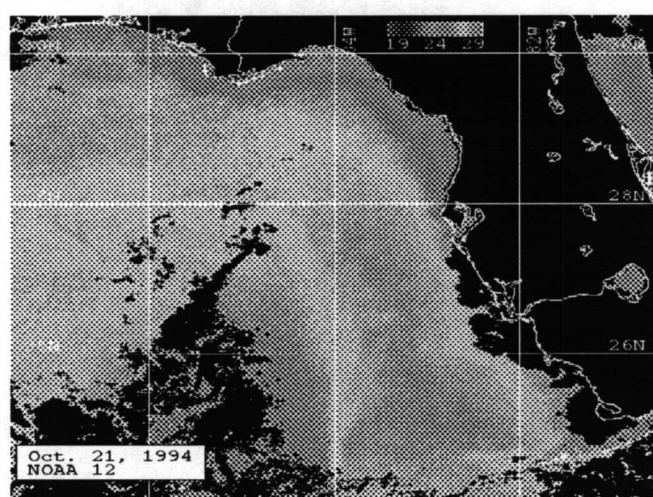


**Figure 31** An SST image of the West Florida Shelf for October 21, 1994 derived from AVHRR imagery

**Examples of Hurricanes and Tropical Storms in the Northeastern Gulf of Mexico:** One of the best set of observations of hurricanes and tropical storms over the northeastern Gulf of Mexico occurred between June and October 1979. During this time, Halper and Schroeder (1990) were monitoring current meters deployed at sites on the Texas Louisiana, Alabama and West Florida Shelves. During the deployment period of these sites, five tropical disturbances (Hurricane Bob, Tropical Storm Claudette, Tropical storm Elena, Hurricane David, Hurricane Frederic, and Hurricane Henri) affected the area.

Hurricane Bob, which passed 620 km to the west of the Florida Middle Ground mooring, provided winds as high as 25 knts. At the mooring off the Alabama coast. When the area was under the influence of the hurricane, the currents in the bottom layer were flowing in opposition to the wind stress.

Tropical Storm Claudette, however, passed directly over the mooring located off of the Texas/Louisiana coast. Remotely, the storm caused a rotation of the surface current vectors from south to north at the Florida Middle Grounds. With the winds blowing a steady north-northwest heading, the maximum currents reached  $\sim 40 \text{ cm s}^{-1}$  and after the passage of the storm, inertial oscillations of  $\sim 20 \text{ cm s}^{-1}$  to  $\sim 25 \text{ cm s}^{-1}$  lasted for 5 days. Closer to the bottom, the flow shifted from a weak flow to the south to a stronger flow to the northwest. The maximum current speeds after this shift in direction reached as high as  $61 \text{ cm s}^{-1}$ .

The most dramatic, recorded response to Claudette occurred off the Texas/Louisiana coast. The mooring measured currents at 60 m and 96m in 100 m of water. With maximum sustained winds of 45 knts., the 28 hour lowpass currents, at the upper mooring, went from an initial state of weak  $5\text{-}10 \text{ cm s}^{-1}$  magnitudes, and then rotated from a westerly to a southerly direction. They then made a rapid shift in direction to the north-northwest and an increase in speed to  $25\text{-}30 \text{ cm s}^{-1}$ . The unfiltered currents reached a maximum of  $55\text{-}60 \text{ cm s}^{-1}$  to the northwest. The filtered series illustrated the generation of intense oscillations at the inertial/diurnal period after the storm passage. These oscillations were accompanied by a  $2^\circ\text{C}$  drop in temperature lasting one day. The near-bottom lowpass flow was to the south prior to the storm. This shifted to the north-northeast and the magnitudes increased  $5 \text{ cm s}^{-1}$  to  $15 \text{ cm s}^{-1}$ . This drop in temperature was also observed and Halper and Schroeder attribute it to upwelling of cold water over the shelf break near the bottom. Inertial oscillations were also observed at this depth.

Tropical Storm Elena and Hurricane David passed through the area at roughly the same time. Elena had little effect, but the effects of David were felt on the Florida Middle Grounds as the hurricane travelled up the east coast of Florida. The 28 hour lowpassed data from the upper current meter, at 9 m in 31 m of water, showed an abrupt shift to the south as David moved up the Atlantic coast. The maximum unfiltered current was  $55 \text{ cm s}^{-1}$  with a maximum of  $40 \text{ cm s}^{-1}$  in the filtered data. The flow was primarily to the south until Hurricane Frederic passed over the mooring less than a week later.

Hurricane Frederic produced estimated maximum sustained winds of 115 knts. The center of the storm passed directly over the Alabama mooring destroying the mooring there. Lowpassed data from the mooring at the Florida Middle Grounds revealed a direction shift from south to the north as the storm entered the Gulf of Mexico east of the Yucatan Channel. The strongest flow was along the isobaths to the north-northwest and had maximum speeds of about  $85\text{-}90 \text{ cm s}^{-1}$ .

At the bottom meter, the flow was slightly to the left of that measured closer to the surface with maximum currents of about  $25\text{-}30 \text{ cm s}^{-1}$ . Inertial oscillations were formed with magnitudes of  $25 \text{ cm s}^{-1}$  and lasted for 5 days. Prior to the arrival of Frederic, the thermocline was near the bottom with a depth range of 23-25 m in 31 m of water. After the storm passage, the water temperature near the bottom had increased  $2\text{-}3^\circ\text{C}$  and a thermocline did not develop for the rest of that summer.

Hurricane Henri showed no appreciable responses at any of the stations. There were inertial oscillations setup at the Texas/Louisiana station which were comparable to the other oscillations previously discussed. The previous mixing of the water column by Hurricane Frederic produced a barotropic response to Henri.

All of these storms setup inertial oscillations and the results from the Florida Middle Ground mooring suggest that the water is set into motion as the storms enter the gulf basin before the winds from the storm present themselves locally. These storms also forced sealevel setup/setdown at the coast which drove the flow response on the shelf as a result of the sealevel gradient and the subsequent relaxation of that setup.

In 1994, Tropical Storm Alberto moved into the Gulf of Mexico in late June. Its passage, on July 2, was marked by 30 knt. winds at the USF mooring located at  $27^\circ 41.4' \text{ N}$ ,  $83^\circ 13.2' \text{ W}$ . The 36 hour lowpassed currents flowed at about  $30 \text{ cm s}^{-1}$  to the north-northeast and then rotated towards the east over the next two days. Inertial oscillations were also observed after the passage of this storm.

The 1995 hurricane season was the most active one in recorded history. There were 21 named storms, and 5 crossed the northeastern Gulf of Mexico. Allison was the first of the season, and was small in scale. The two strongest hurricanes that traversed this area were Erin and Opal. Erin formed over the Bahamas and quickly reached Category 1 strength before reducing to a

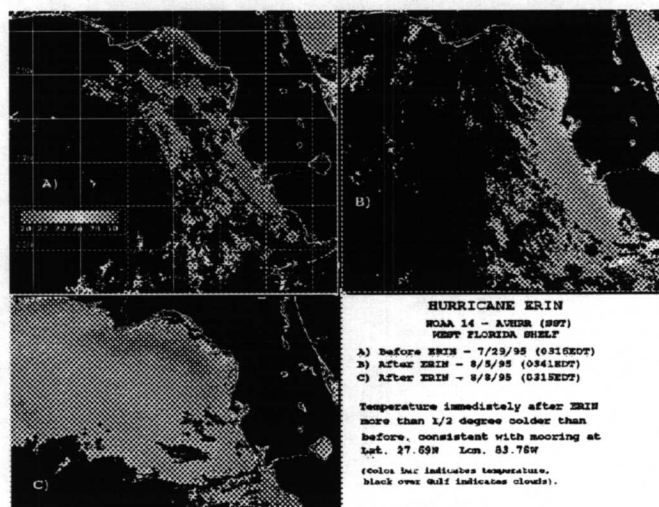


**Figure 32** SST images derived from AVHRR imagery of the West Florida Shelf showing conditions before and after the passage of Hurricane Erin

tropical storm as it crossed the Florida peninsula. After reaching the warm waters of the Gulf of Mexico, it spun back up to hurricane strength and was more organized when it moved inland over Pensacola, Florida. Opal, however, formed over the Yucatan Peninsula of Mexico and moved northward, intensifying from a mild Category 1 hurricane to a Category 4 over the course of 12 hours. It weakened to a Category 3 as it traveled over cooler waters in the northeastern Gulf of Mexico before reaching landfall near Pensacola, Florida.

Data have been collected from a University of South Florida meteorological buoy located at  $27^{\circ} 41.4' N$ ,  $83^{\circ} 13.2' W$  for the period spanning July 25 through August 8 1995. This allows us to study the passage of Hurricane Erin and its effects on the eastern Gulf of Mexico.

Preliminary analyses of the these data suggest that the West Florida Shelf experienced about a  $0.5^{\circ} C$  reduction in sea-surface temperature. The hurricane passage was marked by a 15 mbar drop in barometric pressure and wind speeds around  $12 \text{ m s}^{-1}$  at the buoy. When the *in situ* data (not shown) are compared with NOAA 14 AVHRR images (Figure 32) they seem to be consistent, and this cooling trend is apparent over the whole northeastern Gulf of Mexico. The sea-surface temperature increased about  $1^{\circ} C$  within a couple of weeks.

Although the area presented seemed to cool homogeneously, it did not heat up similarly. The shallows in the Big Bend area showed a sea-surface temperature that was almost a whole degree warmer than the deeper waters offshore. This may be explained by the increased stratification due to the freshwater flux into the area via turbid river runoff and the rainfall delivered by the storm. This stratification will effectively shorten the length of the water column that is heated by the solar radiation. Alternatively, this preferential heating may also be explained by studying the bottom albedo in the Big Bend area. The higher temperatures seem to be confined to the shallows where sea grass is prevalent. These grasses have a darker albedo, thus allowing for the water column to be more efficiently heated. Further studies on the heat budget should be undertaken to better understand the physical processes in this area.

### **Biological Processes:**

#### Seasonal Chlorophyll Pigment Concentration and Sea-surface Temperature Cycles of the Gulf of Mexico:

Introduction: The Gulf of Mexico has been the subject of many physical oceanographic field and modeling studies. Its Loop Current and shedding of large anticyclonic rings are often observed. Less common, however, are studies that concentrate on the biological nature of the Gulf. Monthly climatologies of the sea-surface temperature (SST) and chlorophyll pigment concentrations were used by Walsh et al. (1989) to validate a coupled physical-biological model for the Gulf of Mexico, specifically to model the seasonal biological response to eddy shedding and nutrient injection by the Loop Current, incident light, and vertical mixing. These data were also used by Muller-Karger et al. (1991) in order to examine the spatial and temporal variability of the surface distribution of phytoplankton.

Pigment Concentrations: The Coastal Zone Color Scanner determines the water-leaving radiance at 6 visible and IR bands. Concentrations are derived using ratios of the blue (443 nm)

or blue-green (520 nm) to the green radiance (550 nm) values. Values are obtained using atmospheric correction and bio-optical (derived empirically) algorithms valid for deep, low-chlorophyll waters ( $0.08\text{-}1.5 \text{ mg m}^{-3}$ ). Satellite values provide an estimate of the average pigment concentration in the first water optical depth, which at low concentrations ( $0.04\text{-}0.5 \text{ mg m}^{-3}$ ) represent a layer of 10-25 m in depth. These pigment values have been validated and found to agree within 40% under optimal conditions. Case II waters possess large concentrations of colored dissolved organic matter (Gelbstoff), marine or terrigenous effluent from rivers, or resuspended sediments. Satellite-derived values for pigment concentrations in Case II waters are not as accurate as Case I since phytoplankton do not covary with these other constituents, making the CZCS blue-green ratio algorithm unfeasible. Bio-optical algorithms often overestimate the chlorophyll pigment concentration by attributing the strong signal to pigment when it is due to the presence of other material. As such, the accuracy of retrieved chlorophyll values are questionable over shallow shelf waters and regions of river plume dispersal.

Sea-surface Temperature: Monthly SST images have also been created by Muller-Karger et al. (1991). The global monthly average bias error is less than  $0.1^\circ \text{ C}$ , and the root mean square (rms) error is less than  $0.8^\circ \text{ C}$ . Individual points, however, may be less accurate. The multichannel sea-surface temperature (MCSST) procedure is described in great detail in McClain et al. (1990). Monthly profiles of temperature, salinity, and depth were also created from NOAA National Oceanographic Data Center (NODC) station data.

Sampling Notes: The entire pigment time series extends over the life of the CZCS, from November 1978 to November 1985. Due to scheduling, satellite position, and satellite power drains, 41% of the data examined were collected in just 1979 and the first six months of 1980. Temporal sampling for June 1980 through December 1982 resulted in markedly decreased coverage. Coverage is completely lacking in November 1980, June 1981, April 1984, and May 1985. Cloud cover also aliases time series of pigment fields, since periods of atmospheric frontal passage or storms are far more prevalent during certain yearly periods.

Chlorophyll Characteristics: The CZCS images of monthly mean pigment fields in the Gulf of Mexico from November 1978 through November 1985 have been derived. The CZCS time series of phytoplankton concentration show that seasonal variation in pigment concentration seaward of the shelf is synchronous throughout the Gulf, with highest values ( $> 0.18 \text{ mg m}^{-3}$ ) in December-February, and lowest values ( $\sim 0.06 \text{ mg m}^{-3}$ ) in May-July. This synchronicity may be more clearly seen in a time series of two 200-km square subregions (Figure 33) of the Gulf-- one in an offshore area under Loop Current influence, and the other without (Figure 34). The algal biomass

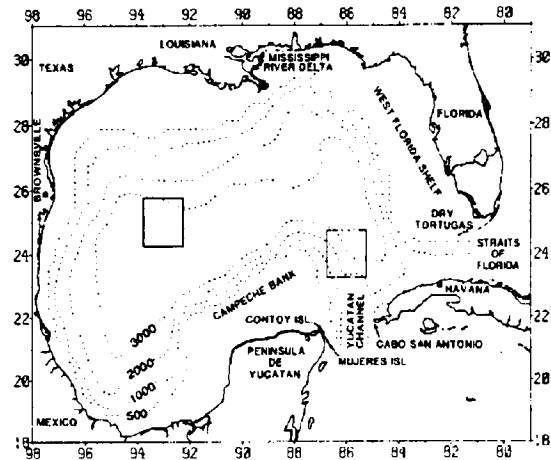


**Figure 33** A map showing the location of two 200-km square subregions of the Gulf of Mexico studied using CZCS

cycles are clearly similar, showing that temporal pigment variability in offshore waters is independent of the Loop Current or the presence of anticyclonic eddies.

It is important to note these time series are robust only up to about 1982; beyond this, artifacts may have been introduced by the drastic decrease in CZCS sampling, such as volcanic eruptions (Mt. Chichon) and sensor instability. The climatologies derived here include this part of the record as well.

**Plume and Loop Current Recognition:** When local processes of wind mixing do not dominate the surface chlorophyll field, CZCS imagery may be used to delineate circulation features of the oligotrophic state of the Gulf of Mexico. For example, the more robust portion of the time series of pigment images show that during summer there was marked spatial structure of low algal biomass associated with the Loop Current and anticyclonic eddies. The eastern Gulf was dominated by the clear-water intrusion of the summer Loop Current, while the western side contained patches of clear water associated with anticyclonic rings of downwelling cores, where nutrient depletion of shallow mixed layers is accentuated during summer periods.

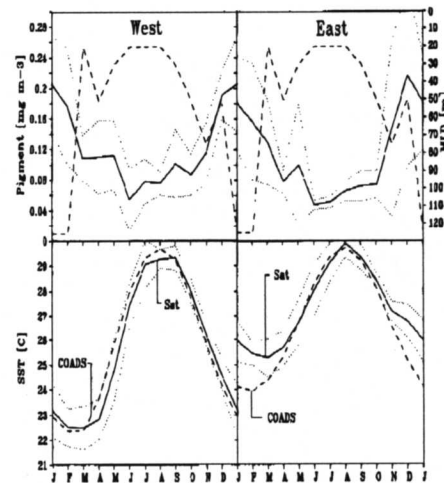


**Figure 34** A monthly climatology of pigment concentration ( $\text{mg pigment m}^{-3}$ ) and SST within the two studied subregions

Pigment field structure disappears in winter, however, as concentrations increase

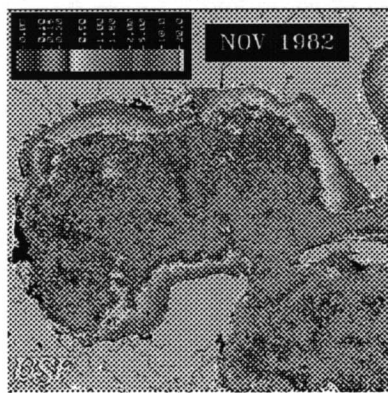


**Figure 35** A monthly composite of chlorophyll pigment concentration derived from CZCS imagery of the Gulf of Mexico for November 1982

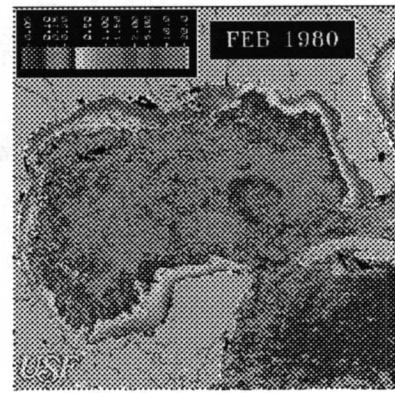


**Figure 36** A monthly composite of chlorophyll pigment concentration derived from CZCS imagery of the Gulf of Mexico for February 1980

simultaneously throughout the Gulf. Offshore pigment fields become horizontally homogeneous as early as November, as seen in Figure 35, and do not develop significant spatial structure again until about February of the following year, shown in Figure 36. The ocean color images show that most of the water discharged by the Mississippi River flows to the west, following the Louisiana-Texas coast, at times reaching south of the border between Mexico and the United States of America. For example, the CZCS composites for 1979 and 1980 show that most of the Mississippi River discharge was carried west in a band following the coast and extending at least as far as Tampico, Mexico. There were no apparent seasonal changes in the direction of the dispersal of the plume. However, there were large interannual differences in the size of the plume (length and width) consistent with variations in volume discharge.

**Biological Productivity:** The biological productivity of the shelf is strongly affected by Mississippi River effluent, outflow from coastal lagoons and smaller rivers, cyclonic eddies which develop along the continental margin, and wind-driven upwelling through the mixed layer (Walsh, 1988).

A dearth of nutrient and primary productivity observations for the Gulf of Mexico make estimation of the relative contribution of nutrient supply mechanisms difficult. The following points may be noted to form a picture of the processes leading to the observed chlorophyll pigment patterns:

- During a quasi-annual penetration and eddy shedding cycle of the Loop Current, the simulated seasonal changes of incident light, winds, and surface mixed layer depth from Levitus (1982) induce an annual cycle of algal biomass that correspond will to *in situ* and satellite time series of chlorophyll. The modeled phytoplankton concentrations were highest when the mixed layer was deepest (100 m) and reached a minimum simultaneously with the shallowest mixed layer (25 m), such that flux minima occur during periods of greatest water stratification.
- Surface wind stress dictates the depth of the model's surface mixed layer: both are greatest in the winter months (November to March).
- Maximal chlorophyll concentrations are found from November to January beyond the shelf break.
- Maximum northward penetration of the Loop Current occurs in March, April, and May (Vukovich 1979).
- Riverine input is often high in chlorophyll, nutrients, and dissolved organic matter; Figure 37 shows Mississippi River outflow is greatest during spring (January-March). Thus, as winds increase and air temperature drops in early winter, the surface mixed layer deepens due to heat loss and convective overturn, increasing the nutrient supply and pool. Enhanced autumn river discharge also aids in phytoplankton growth and supply to the Gulf waters. During the winter, phytoplankton growth flourishes with maximal nutrient availability that is further enhanced by the northward penetration in early spring by the Loop Current, promoting upwelling in the surrounding waters and nutrient supply from deep water. Growth is also enhanced by the increased spring river outflow that is high in chlorophyll and nutrients. Then, as spring moves to summer, the Loop Current retreats,

cutting off nutrient supply from upwelling, river outflow decreases, and winds die, shallowing the surface mixed layer. All these factors lead to a decreased nutrient supply and pool, inhibiting phytoplankton growth. These reasons combine to explain the lower phytoplankton concentrations found during the summer months.

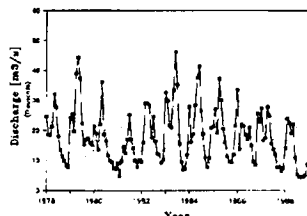


**Figure 37** A time series of monthly discharge ( $\text{m}^3 \text{s}^{-1}$ ) values for the Mississippi River as measured at Vicksburg, MS

**Weekly SST Composites:** Weekly SST composites have been created from AVHRR images from late 1993 through the first half of 1996. The SST changes were synchronous between the eastern and western portions of the Gulf. Spatial SST structure in the AVHRR images are poorly developed during summer (May through October) but very well developed from November through May. Thus, infrared satellite images provide synoptic maps of the Loop Current and its eddies only during a 7-month period of the year. The remainder of the year sees an insufficient temperature gradient that makes identifying the Loop Current from IR imagery impossible.

**SST and Pigment Concentration Complementary:** The combined use of ocean color and infrared images permits year-round observation of spatial structure of the surface circulation in the Gulf. Thermal infrared images are most useful between November and mid-May, when strong temperature gradients occur. The SST fields are uniform between late May and October, but the Loop Current, large anticyclonic eddies, and Mississippi River plume may be traced with chlorophyll pigment concentrations using ocean color sensors.

Despite many oceanographic studies of the Gulf of Mexico, questions of the processes controlling ring and eddy formation or frequency of eddy shedding, for example, remain unanswered. Satellite observations on a year-round basis will soon become possible with the upcoming launches of the Japanese Ocean Color Temperature Sensor (OCTS) and SeaWiFS. These observations will provide an unparalleled glimpse of the processes governing the Gulf of Mexico.

### River Plume Productivity:

**Introduction:** A close examination of the Coastal Zone Color Scanner (CZCS) data shows the episodic formation of a high pigment plume in the northern part of the West Florida Shelf during spring. The degradation of this spring bloom to organic and inorganic materials may lead to subsequent fall blooms of dinoflagellates within the inner shelf waters of central Florida. Gilbes et al. (1996) have observed this phytoplankton plume, which has remained undetected by other investigators as a result of infrequent ship surveys. It extends southward from Cape San Blas toward the Florida Keys along the shelf break. The regular occurrence of this plume may support the idea that energy transfer to higher trophic levels on the northern part of the West Florida Shelf is seasonal.

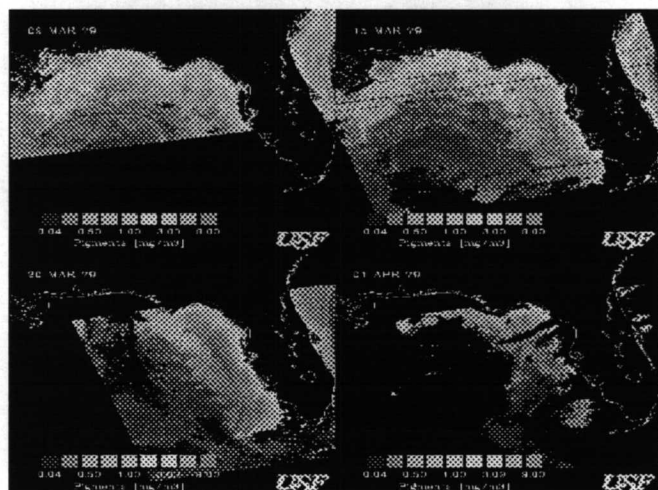


**Figure 38** A CZCS time series of the West Florida Shelf showing the formation of the West Florida plume during March 1979

In 1980, the plume on the West Florida Shelf had maximum concentrations in May and a duration of approximately one month as shown in Figure 42. The plume was first detected off Cape San Blas on April 24 (Figure 43), with pigment concentrations  $>0.5 \text{ mg m}^{-3}$ , while further south the pigment concentration remained low ( $0.1\text{--}0.2 \text{ mg m}^{-3}$ ). In Figure 44, we see that on May 16, a well-defined plume extended southward with values up to  $5.0 \text{ mg m}^{-3}$ . On May 19 (Figure 45), pigment concentrations decreased to  $<2.0 \text{ mg m}^{-3}$ . The plume disappeared on June 2 ( $<0.25 \text{ mg m}^{-3}$ ).

**Occurrence and Lifetime of the West Florida Plume:** In 1979, the West Florida plume, shown in Figure 38, occurred during March, and it lasted at least two weeks. The plume was first detected on March 9, when pigment concentrations were between  $0.5$  and  $1.0 \text{ mg m}^{-3}$ . On March 15 (Figure 39), the plume extended southward from Cape San Blas along the shelf with pigment values between  $2.0$  and  $5.5 \text{ mg m}^{-3}$ . Pigment concentrations were between  $1.0$  and  $2.0 \text{ mg m}^{-3}$  on March 20 (Figure 40) and  $<0.5 \text{ mg m}^{-3}$  on April 1 (Figure 41).

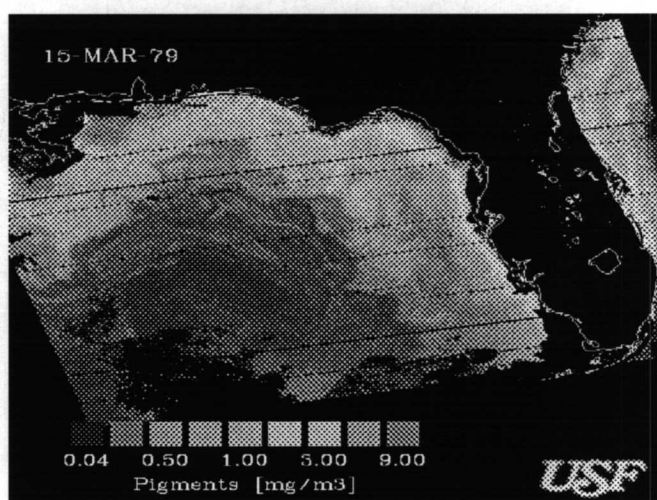


**Figure 39** A CZCS image of the West Florida Shelf showing the West Florida Plume on March 15, 1979

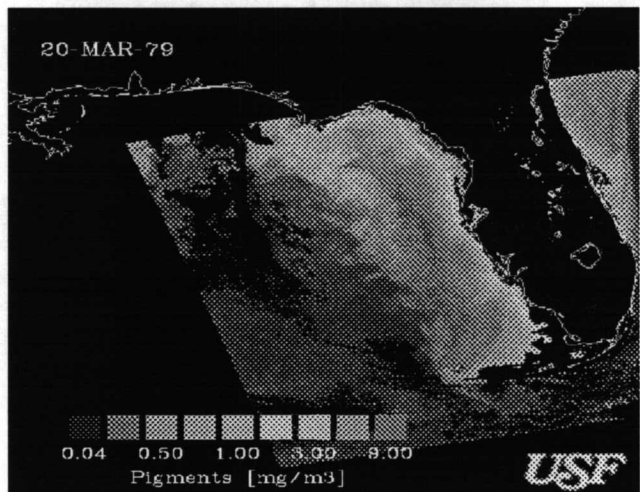


**Figure 40** A CZCS image of the West Florida Shelf showing the West Florida plume on March 20, 1979

In 1986, the maximum concentrations of the West Florida plume was observed in March and it lasted about a month. In mid-January, coastal waters off Cape San Blas began showing

Similar plumes on the West Florida Shelf were detected in CZCS imagery between 1981 and 1986. However, the number of usable images during these years was lower than in previous years, making the analysis of the time sequence of the plumes more difficult. A reduction in CZCS operational time plus cloud cover were the major reasons for decreased coverage. A plume with pigment concentrations  $>0.5 \text{ mg m}^{-3}$  was identified in February 1981, shown in Figure 46, February 1982, shown in Figure 47, May 1983, shown in Figure 48, April 1984, shown in Figure 49, May-June 1985, shown Figure 50, and March 1986, shown in Figure 51. The duration of the plume for those years varied from one week to one month.

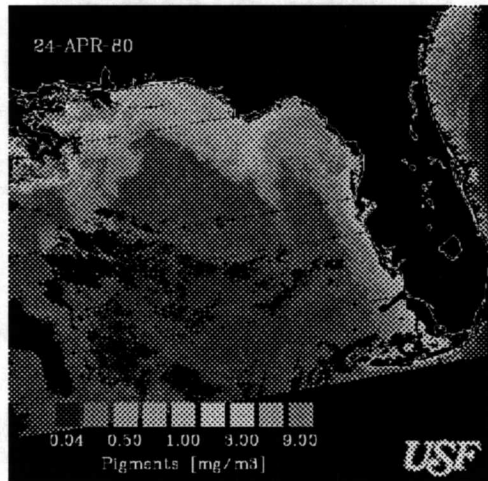


**Figure 43** A CZCS image of the West Florida Shelf showing the West Florida plume on April 24, 1980

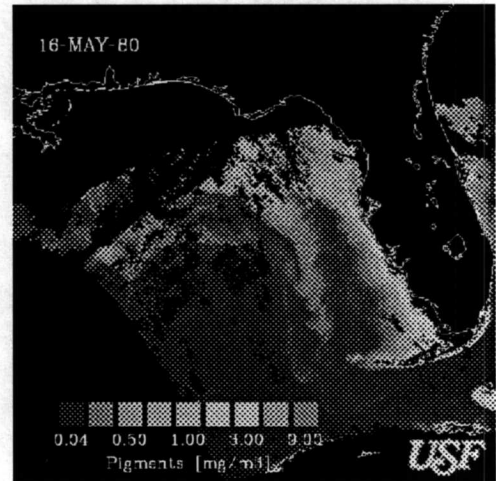


**Figure 44** A CZCS image of the West Florida Shelf showing the West Florida Plume on May 16, 1980

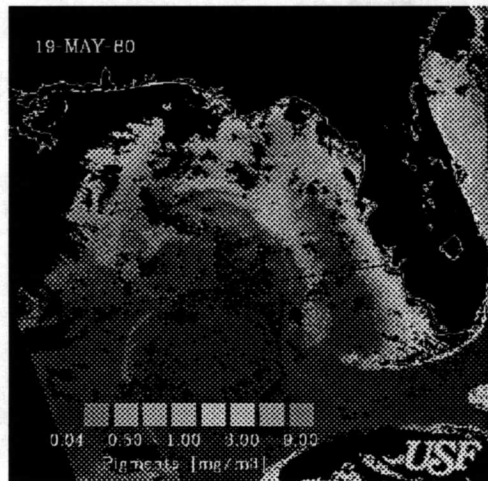


**Figure 45** A CZCS image of the West Florida Shelf showing the West Florida plume on May 19, 1980

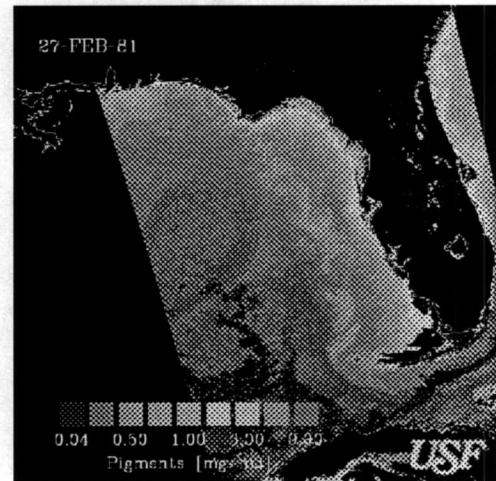


**Figure 46** A CZCS image of the West Florida Shelf showing the West Florida plume on February 27, 1981

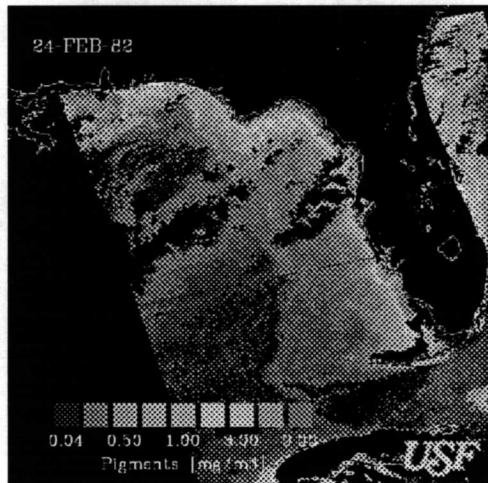


**Figure 47** A CZCS image of the West Florida Shelf showing the West Florida plume on February 24, 1982

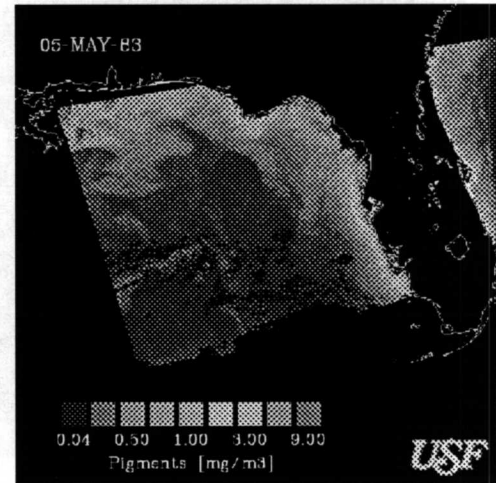


**Figure 48** A CZCS image of the West Florida Shelf showing the West Florida plume on May 5, 1983

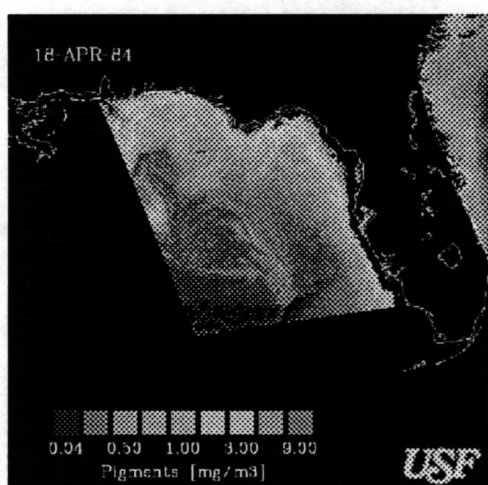


**Figure 49** A CZCS image of the West Florida Shelf showing the West Florida plume on April 18, 1984

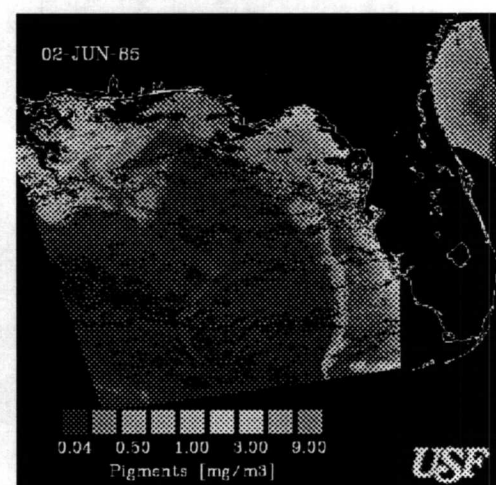


**Figure 50** A CZCS image of the West Florida Shelf showing the West Florida plume on June 2, 1985

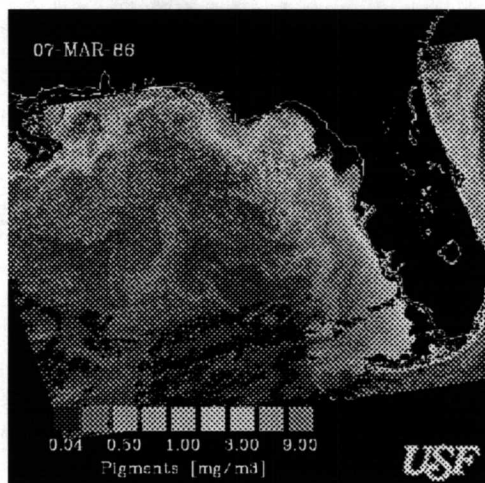


**Figure 51** A CZCS image of the West Florida Shelf showing the West Florida plume on March 7, 1986

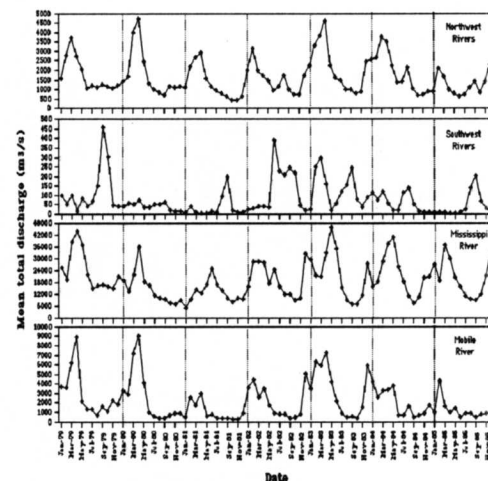


**Figure 52** Mean total discharge ( $\text{m}^3 \text{s}^{-1}$ ) for the rivers on the northwest coast of Florida, the southwest coast of Florida, the Mississippi River and the Mobile River for 1979 - 1985

**Processes Responsible for the Formation of the West Florida Plume:** While the periodic occurrence of the chlorophyll plumes is confirmed by in situ and satellite data, the processes responsible for the formation of these plumes remain unclear. Gilbes et al. (1996) found that such plumes may be related to one or a combination of the following factors: (1) discharge from small, local rivers along the northwest Florida coast; (2) seasonal changes in steric height differences between the shelf and deep Gulf of Mexico waters; (3) circulation of water associated with the Loop Current and upwelling in the De Soto Canyon; and (4) discharge from the Mississippi and Mobile Rivers.

**Local Rivers:** The Gulf coast of Florida receives the discharge of 21 rivers, primarily concentrated in the northern region. Although it has been demonstrated that the runoff of these rivers affects the chemistry and biology of estuarine zones, their impact on shelf waters is unclear. The northwest Florida rivers (Perdido, Escambia, Blackwater, Yellow, Choctawhatchee, Econfina Creek, Apalachicola, Ochlockonee, Aucilla, Encofina, Fenholloway, Steinhatchee and Suwannee Rivers) showed maximum and minimum discharge during spring and fall, respectively (Figure 52). Peak discharge during spring coincided with the appearance of the West Florida plumes in the CZCS images. The southwest Florida rivers (Withlacoochee, Hillsborough, Alafia, Little Manatee, Manatee, Myakka and Peace Rivers) showed more irregularity, but in general the maximum discharge was during summer-fall. The high seasonal discharge of the northwestern rivers can represent a source of inorganic nutrients for the formation of the West Florida plume. Gilbes et al. (1996) examined the inorganic nitrogen loading for the Apalachicola, Suwannee, Escambia, and Choctawhatchee Rivers. The inorganic nitrogen loading during winter-spring

(January to June) was about two times higher than during summer-fall (July to December). High pigment concentrations ( $>0.5 \text{ mg m}^{-3}$ ) at northWest Florida Shelf showed a correspondence with high nitrogen loading during March 1979, November 1980, and March 1981.

Water Circulation: A recent study suggests that southward circulation on the West Florida Shelf is produced by differential heating and cooling within different regions (Robert Weisberg, personal communication). The Loop Current has a significant year-round effect on maintaining a higher temperature offshore relative to waters on the West Florida Shelf. Calculations of steric height differences show that the sea level at a shelf location can be between 27 and 33 cm lower than an offshore location at the same latitude. These differences generate a pressure gradient toward the shore that will be balanced by Coriolis. Assuming a barotropic condition, the water mass will therefore move southward, with the strength of the flow proportional to the differences in steric height. Southward movement of shelf waters may transport phytoplankton, nutrients, dissolved organic matter, and suspended sediments from northern to central and southern regions. As this effect would have a maximum in the February-April timeframe, coinciding with the spring maximum discharge of rivers into the Northern Gulf, the southward plumes detected along the West Florida Shelf may be caused by this type of circulation.

Loop Current Intrusions: Nutrient supply associated with upwelling caused by intrusion of the Loop Current to the Southwest Florida Shelf is restricted to the outer shelf. In contrast, on the Northwest Florida Shelf, large intrusions of the Loop Current affect shelf waters to within a few kilometers of the beach. Some researchers have suggested that "the canyon may have been a conduit for the northward flow of deep gulf waters." Previous observations suggest that an episodic upwelling through the De Soto Canyon may provide nutrient injections to the inner West Florida Shelf from deep offshore waters. During January and February of 1992, the Loop Current intruded as far as  $29^{\circ}$  North into the Gulf of Mexico. This intrusion could thus have reached the DeSoto Canyon, supplying nutrients from deep waters. The phytoplankton communities of Northwest Florida may have responded to this input during March 1992. However, there is insufficient information to quantitatively evaluate the role of the DeSoto Canyon and the Loop Current on episodic nutrient supply; more research is required.

Mississippi and Mobile Rivers' Discharge: The discharge of the Mississippi and Mobile Rivers represents a possible source of "Colored Organic Matter (COM)" on the West Florida Shelf. The Mississippi River ranged from  $4,932$  to  $45,960 \text{ m}^3 \text{ s}^{-1}$  and the Mobile River ranged from  $282$  to  $9,018 \text{ m}^3 \text{ s}^{-1}$  during 1979-1985. Both rivers showed high and low discharge during spring and summer, respectively. The high discharge in spring coincides with high pigment concentrations and the occurrence of the West Florida plumes detected by the CZCS at that time. However, the seasonal correspondence between discharge and pigments was not as good as with the northwest Florida rivers. Several studies show that the Mississippi River outflow can move toward the southeast and become entrained in the eastern edge of the Loop Current. The episodic northward intrusions of the Loop Current during winter and spring can transport low-salinity and chlorophyll a/COM rich waters from the Mississippi and Mobile rivers to the

West Florida Shelf. This occasional eastward transport to the West Florida Shelf may be added to the input of local rivers and Loop Current induced upwelling, all producing good conditions for phytoplankton growth and biomass accumulation.

Summary: The complexity of the West Florida Shelf has been demonstrated with the CZCS and field data. An initial diatom spring bloom may originate in waters off northwest Florida, due mainly to the input of nutrients from local river discharge. Intrusions of the Loop Current may induce both upwelling in the DeSoto Canyon and eastward transport of effluents from the Mississippi and Mobile Rivers. Shelf circulation patterns induced by steric height differences can move the phytoplankton and other suspended organic material southward. Still, these processes are poorly understood. Future studies in the West Florida Shelf must provide more spatial and temporal field data in order to elucidate the relationship between phytoplankton processes, dissolved organic carbon, inherent and apparent optical properties, and water circulation. The next generation of ocean color sensors will provide the synoptic view.

**Geological Processes:** Satellite SST imagery is an effective tool in recognizing surface circulation patterns, but when coupled with *in situ* measurements, its ability for describing the horizontal flow structure is improved. Remote Sensing of Geological Processes, suspended matter concentrations and patterns change very rapidly as tides, winds, and river discharge fluctuate. This strong variability complicates interpretation of remotely sensed information regarding estuarine circulation, transport and distribution of river discharge, and mixing processes. The frequent sampling required, however, to resolve tidal effects cannot be provided by data from polar-orbiting spacecraft. These data must be supplemented with more frequent acquisitions from aircraft, buoys, drifters, and ships. Satellite sensors can, however, provide global access to remote areas where coastal processes can be imaged synoptically. Sediment load in the water greatly regulates the primary production of seagrasses and phytoplankton by strongly affecting light availability within the water column. Estimates of the diffuse attenuation coefficient K and its correlation to the reflectance of the water allow some prediction to be made of the light field within a sediment-loaded environment. Suspended sediments may also act as "tracers" (streak lines) that reveal circulation patterns in areas where sea-surface temperature and/or chlorophyll pigment concentration may not be readily apparent or recoverable.

The turbidity of the water controls the total reflectance leaving the water. Thus, river discharge generally high in terrigenous material and degradation products from primary productivity may be observed with sensors possessing a high saturation radiance such as the AVHRR. Due to the high frequency sampling of the AVHRR, detailed pictures of the time evolution of plumes in the Mississippi Delta and Mobile Bay are available with Figures 53,54,55,56 presented as an example of one such evolution.

Stumpf and Tyler (1988) have constructed a model that estimates seston concentration from the received radiances, assuming the absorption and scattering characteristics of the suspended particles are known. These properties are specific to a region and time of year; thus, the application of such a model needs to be carefully performed. One such survey has been performed for a spring Mobile Bay plume. Images of the spring Mobile Bay plume (Apr 3, pm; Apr 4, am; Apr 4, pm; Apr 5, am; and Apr 5, pm) are offered in Figures 57 - 61. In such imagery, the rapid changes in sediment load in the water is apparent. Further information may be obtained in Stumpf and Pennock (1991) and Stumpf and Tyler (1989).



**Figure 53** Reflectance of the Mobile Bay region measured using AVHRR for March 24, 1990

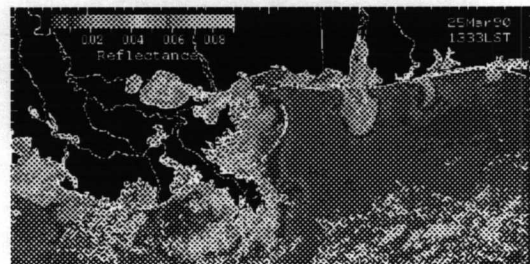


**Figure 54** Reflectance of Mobile Bay region measured using AVHRR for March 25, 1990

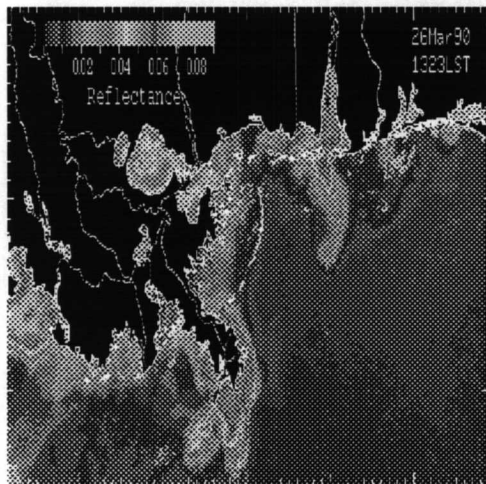


**Figure 55** Reflectance of the Mobile Bay region measured using AVHRR for March 26, 1990

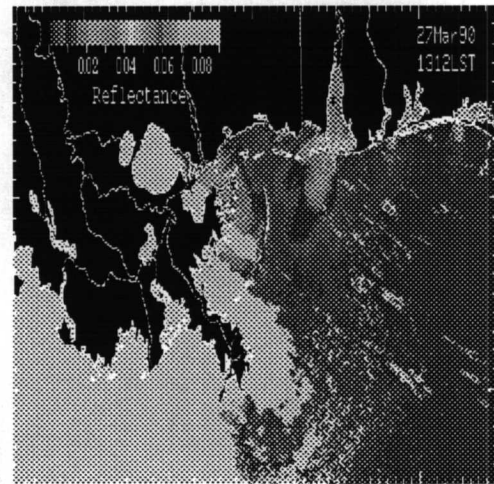


**Figure 56** Reflectance of the Mobile Bay region measured using AVHRR for March 27, 1990

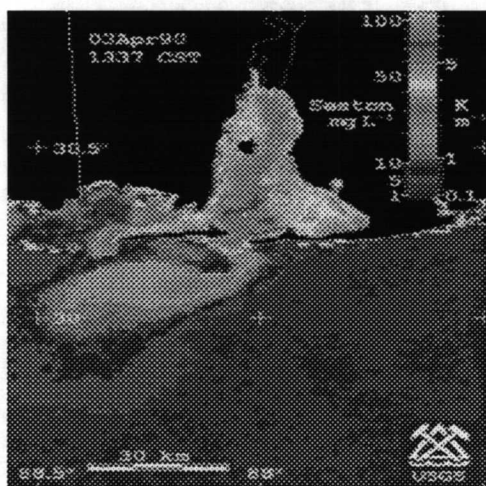


**Figure 57** Suspended sediment load of the Mobile Bay region derived from afternoon AVHRR images for April 3, 1990

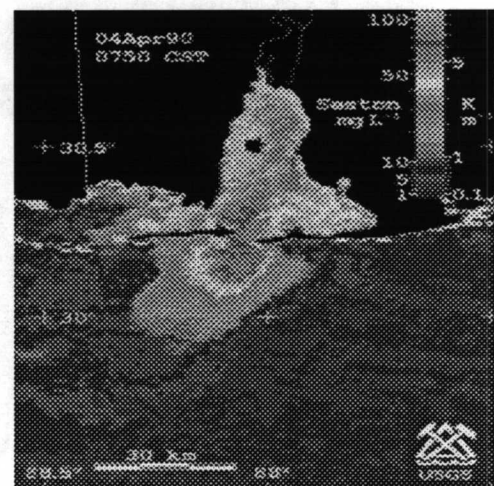


**Figure 58** Suspended sediment load of the Mobile Bay region derived from morning AVHRR images for April 4, 1990

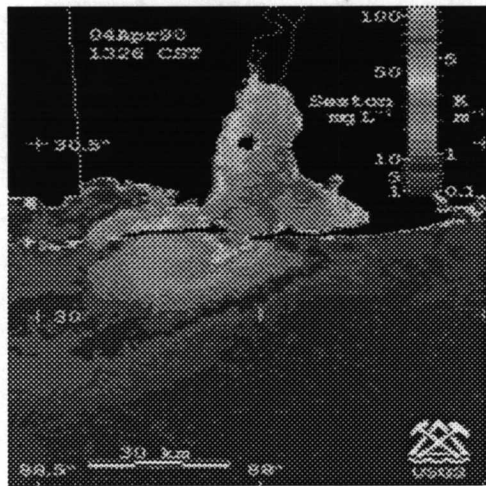


**Figure 59** Suspended sediment load of the Mobile Bay region derived from afternoon AVHRR images for April 4, 1990

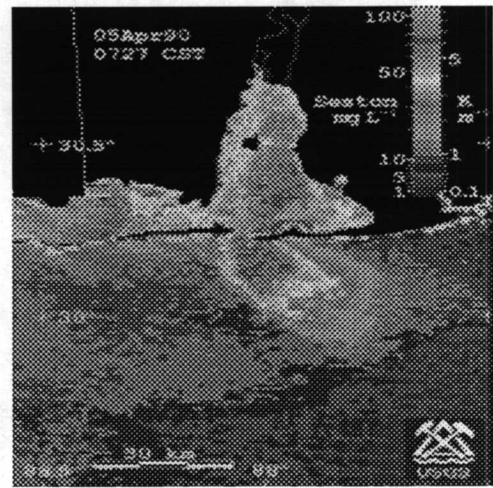


**Figure 60** Suspended sediment load of the Mobile Bay region derived from morning AVHRR images for April 5, 1990

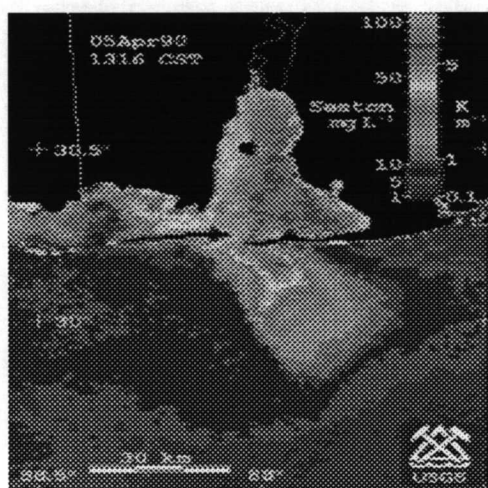


**Figure 61** Suspended sediment load of the Mobile Bay region derived from afternoon AVHRR images for April 5, 1990

## References

- Andersen, O.B. (1994) "Ocean tides in the northern North Atlantic and adjacent seas from ERS 1 altimetry," *J. Geophys. Res.* 99(C11): 22,557-22,573.
- Carder, K. L., P. Reinersman, et al. (1993) "AVIRIS calibration and application in coastal oceanic environments," *Remote Sensing of the Environment* 44: 205-216.
- Fu, L-L., et al. (1994) "TOPEX/POSEIDON mission overview," *J. Geophys. Res.* 99(C12): 24,369-24,381.
- Gordon, H. R. and D. K. Clark (1981) "Clear water radiances for atmospheric correction of coastal zone color scanner imagery," *Applied Optics* 20(24): 4,175-4,179.
- Gordon, H. R., et al. (1983) "Phytoplankton pigment concentrations in the Middle Atlantic Bight: comparison of ship determinations and CZCS estimates," *Applied Optics* 22(1): 20-36.
- Halper, F. B. and W. W. Schroeder (1990) "The response of shelf waters to the passage of tropical cyclones- observations from the Gulf of Mexico," *Continental Shelf Res.* 10(8), 777-793.
- Heywood, K.J. (1994) "Eddy kinetic energy of the North Atlantic subpolar gyre from satellite altimetry," *J. Geophys. Res.* 99(C11): 22,525-22,539.
- Levitus, S. (1982) Climatological Atlas of the World Ocean, Environmental Research Laboratories, Geophysical Fluid Dynamics Laboratory, Princeton, NJ., U.S. Department of Commerce, NOAA Professional Paper 13, 173 pp.
- Levitus, S. (1982) Climatological atlas of the world ocean, Tech. Pap., 3, 173 pp., Natl. Oceanic and Atmos. Admin., Silver Spring, MD.
- Maul, G. A. (1977) The annual cycle of the Gulf Loop Current, I, Observations during a one-year time series, *J. Mar. Res.*, 35(1): 29-47.
- Maul, G. A., et al. (1985) "Comparisons between a continuous 3-year current-meter observation at the sill of the Yucatan Strait, satellite measurements of Gulf Loop Current area, and regional sea level," *J. Geophys. Res.* 90(C5): 9,089-9,096.

- McClain, C. R., W. E. Esaias, G. C. Feldman, J. Elrod, D. Endres, J. Firestone, M. Darzi, R. Evans, and J. Brown (1990) Physical and biological processes in the North Atlantic during the first GARP global experiment, *Journal of Geophysical Research*, 95(C10): 18,027-18,048.
- McClain, E. P., W. G. Pichel, and C. C. Walton (1985), Comparative performance of AVHRR based multichannel sea-surface temperatures, *J. Geophys. Res.*, 90(C6): 11,587-11,601.
- Muller-Karger, F.E., et al. (1991) "On the seasonal phytoplankton concentration and sea-surface temperature cycles of the Gulf of Mexico as determined by satellites," *J. Geophys. Res.* 96(C7): 12,645-12,665.
- Pickard, G. L. and W. J. Emery (1990) Descriptive physical oceanography: an introduction 5th ed., Pergamon Press, 320 pp.
- Semtner, A.J., and R. M. Chervin (1992) "Ocean general circulation from a global eddy-resolving model," *J. Geophys. Res.* 97: 5,493-5,550.
- Stammer, D. and Wunsch, C. (1994) "Preliminary assessment of the accuracy and precision of TOPEX/POSEIDON altimeter data with respect to the large-scale ocean circulation," *J. Geophys. Res.* 99(C12): 24,584-24,604.
- Stommel, H. (1965) The Gulf Stream: a physical and dynamical description. Los Angeles, California, University of California Press.
- Stumpf, R. P. and M. A. Tyler (1988) Satellite detection of bloom and pigment distributions in estuaries, *Rem. Sensing of Environment*, 24: 385-404.
- Sturges, W. (1994) The frequency of ring separations from the Loop Current, *J. Phys. Oc.*, 24(7): 1,647-1,652.
- Walsh, J. J., D. A. Dieterle, et al. (1989) "Nitrogen exchange at the continental margin: a numerical study of the Gulf of Mexico," *Progress in Oceanography* 23: 245-301.
- Walsh, J. J. (1988) On the nature of continental shelves, Academic Press, 508 pp.
- Weisberg, R.H., B.D. Black and H. Yang (1996) Seasonal modulation of the west Florida continental shelf circulation, *Geophys. Res. Lett.*, 23: 2,247-2,250.
- Wick, G.A. and Emery, W.J. (1992) "A comprehensive comparison between satellite-measured skin and multichannel sea-surface temperature," *J. Geophys. Res.* 97(C4): 5,569-5,596.



### The Department of the Interior Mission

As the Nation's principal conservation agency, the Department of the Interior has responsibility for most of our nationally owned public lands and natural resources. This includes fostering sound use of our land and water resources; protecting our fish, wildlife, and biological diversity; preserving the environmental and cultural values of our national parks and historical places; and providing for the enjoyment of life through outdoor recreation. The Department assesses our energy and mineral resources and works to ensure that their development is in the best interests of all our people by encouraging stewardship and citizen participation in their care. The Department also has a major responsibility for American Indian reservation communities and for people who live in island territories under U.S. administration.

### The Minerals Management Service Mission

As a bureau of the Department of the Interior, the Minerals Management Service's (MMS) primary responsibilities are to manage the mineral resources located on the Nation's Outer Continental Shelf (OCS), collect revenue from the Federal OCS and onshore Federal and Indian lands, and distribute those revenues.

Moreover, in working to meet its responsibilities, the **Offshore Minerals Management Program** administers the OCS competitive leasing program and oversees the safe and environmentally sound exploration and production of our Nation's offshore natural gas, oil and other mineral resources. The **MMS Royalty Management Program** meets its responsibilities by ensuring the efficient, timely and accurate collection and disbursement of revenue from mineral leasing and production due to Indian tribes and allottees, States and the U.S. Treasury.

The MMS strives to fulfill its responsibilities through the general guiding principles of: (1) being responsive to the public's concerns and interests by maintaining a dialogue with all potentially affected parties and (2) carrying out its programs with an emphasis on working to enhance the quality of life for all Americans by lending MMS assistance and expertise to economic development and environmental protection.

